Journal of Geophysical Research: Space Physics

TECHNICAL REPORTS: METHODS

10.1029/2018JA025786

Determination of the Equatorial Electron Differential Flux From Observations at Low Earth Orbit

Hayley J. Allison[1,2], **Richard B. Horne**[1], **Sarah A. Glauert**[1], **and Giulio Del Zanna**[2]

[1]British Antarctic Survey, Cambridge, UK, [2]Department of Applied Mathematics and Theoretical Physics, University of Cambridge, Cambridge, UK

Key Points:
- Integral electron flux data from SEM-2 in low Earth orbit are converted to flux energy distributions at 90 degrees equatorial pitch angle
- Two methods to convert from integral to differential flux are explored
- Results validated against Van Allen Probes data show an average agreement for 100-600 keV electrons within a factor of 4 when $L^* > 3.7$

Correspondence to:
H. J. Allison,
haylis@bas.ac.uk

Citation:
Allison, H. J., Horne, R. B., Glauert, S. A., & Del Zanna, G. (2018). Determination of the equatorial electron differential flux from observations at low Earth orbit. *Journal of Geophysical Research: Space Physics*, *123*, 9574–9596. https://doi.org/10.1029/2018JA025786

Received 14 JUN 2018
Accepted 31 OCT 2018
Accepted article online 5 NOV 2018
Published online 13 NOV 2018

Abstract Variations in the high-energy relativistic electron flux of the radiation belts depend on transport, acceleration, and loss processes, and importantly on the lower-energy seed population. However, data on the seed population is limited to a few satellite missions. Here we present a new method that utilizes data from the Medium Energy Proton/Electron Detector on board the low-altitude Polar Operational Environmental Satellites to retrieve the seed population at a pitch angle of 90°. The integral flux values measured by Medium Energy Proton/Electron Detector relate to a low equatorial pitch angle and were converted to omnidirectional flux using parameters obtained from fitting one or two $\sin^N \alpha$ functions to pitch angle distributions given by three and a half years of Van Allen Probes data. Two methods to convert from integral to differential flux are explored. One utilizes integral and differential flux energy distributions from the AE9 model, the second employs an iterative fitting approach based on a Reverse Monte Carlo (RMC) method. The omnidirectional differential flux was converted to an equatorial pitch angle of 90°, again using statistical pitch angle distributions from Van Allen Probe data. We validate the resulting 90° flux for 100- to 600-keV electrons against measurements from the Van Allen Probes and show an average agreement within a factor of 4 for $L^* > 3.7$. The resulting data set offers a high time resolution, across multiple magnetic local time planes, and may be used to formulate event-specific low-energy boundary conditions for radiation belt models.

1. Introduction

Recent work has highlighted the observed links between increases in the seed population (30- to 500-keV electrons) and the generation of relativistic electrons in the Earth's radiation belts (Boyd et al., 2016; Jaynes et al., 2015). Substorm injections can increase the seed population, providing additional electrons that can be accelerated to relativistic energies, potentially resulting in larger relativistic flux levels (Obara et al., 2000). Using the DREAM3D diffusion model, Tu et al. (2014) showed that model results were closer to observations for the October 2012 storm when a realistic seed population was used for the low-energy boundary and event-specific diffusion coefficients were employed. Tu et al. (2014) effectively demonstrated that knowledge of the seed population is important to fully understand the evolution of the radiation belts.

At present, the Van Allen Probes Magnetic Election Ion Spectrometer (MagEIS) provides measurements of the energetic electron flux throughout the Earth's radiation belt region. The twin Van Allen Probes operate in a highly elliptical near-equatorial orbit, with a period of ~9 hr and an apogee of ~5.8 R_E, inside geostationary orbit (Mauk et al., 2013). The level 3 data from MagEIS supplies the electron flux for energies in the range ~30 keV to 4 MeV in 11 pitch angle bins (Blake et al., 2013). The MagEIS instruments were powered on in September 2012 and remain in operation (Spence et al., 2013), providing an excellent data set with which to study the seed population. For radiation belt models, the Van Allen Probes data can be used to create event-specific low-energy boundary conditions in order to examine periods after September 2012. However, before this period, seed population data tend to be limited in energy and pitch angle coverage.

Prior to 2012, the National Oceanic and Atmospheric Administration (NOAA) Polar Operational Environmental Satellites (POES) were operational. The POES satellites carry the Space Environment Monitor (SEM-2) Medium Energy Proton and Electron Detector (MEPED), which measures >30-, >100-, and >300-keV electron data at a 2-s resolution (Evans & Greer, 2004). Launched in May 1998, NOAA15 was the first POES satellite to carry SEM-2. Since then, a further four POES satellites have been launched and, to date, three POES satellites are still sampling data. POES MEPED measurements are therefore available for more than the last 19 years, providing

a wealth of information on seed population electrons. Operating in a ~98.5° inclination low Earth orbit, these satellites sample the electron flux across a broad range of the magnetic coordinate L* (Roederer, 1970). During quiet conditions, POES coverage can extend from L* < 1.3 to L* > 8.5; a larger L* range than possible with the Van Allen Probes. Due to the orbit, the POES satellites offer very rapid measurements of the radiation belts and, with up to five satellites sampling the region, provide data in multiple magnetic local time (MLT) planes. However, one of the major limitations of the POES data set for studying the seed population is that the electron channels of MEPED only supply integral flux. Additionally, measurements are taken near the bottom of magnetic field lines, and the electron flux sampled is consequently of low equatorial pitch angle. If the POES MEPED data set could be used to determine the differential flux at a number of seed population energies, for equatorial pitch angles close to 90°, it could provide detailed information of the seed population prior to the Van Allen Probes mission (September 2012) and form event-specific low-energy boundary conditions for radiation belt models when MagEIS data are unavailable.

In this paper we provide a method to determine the differential electron flux for energies mainly in the 100- to 600-keV range, at a 90° equatorial pitch angle, from measurements taken by the integral electron channels of MEPED onboard the POES satellites at low Earth orbit. Such a task has two main challenges, the first of which involves inferring the state of the energetic electron component of the radiation belts using the low equatorial pitch angle data measured by the POES satellites. In section 3 we present a method to convert the electron flux from the POES satellites to omnidirectional flux, using statistical pitch angle distributions determined from Van Allen Probes measurements. The second main challenge involves using integral flux measurements to deduce the electron flux at a number of seed population energies. Two different methods are explored here, the first of which uses data from the AE9 model, discussed in section 4.1, and the second employs an iterative approach based on what is referred to as a *Reverse Monte Carlo (RMC) method* (McGreevy, 2001), discussed in section 4.2. The omnidirectional flux for a range of energy values are finally converted to directional 90° flux, using the technique presented in section 5. In order to validate the results, we compare the outputs at various energies (100–600 keV) to observations from the Van Allen Probes, the results of which are given in section 6. It is suggested that the methods presented in this paper could be used to formulate event-specific minimum-energy boundary conditions for radiation belt models, using MEPED flux measurements, in order to better study times, or L* values, outside the Van Allen Probes mission. We investigate this idea in sections 7 and 8. Finally, successes and drawbacks of the method are discussed and conclusions presented in sections 9 and 10, respectively.

2. POES Satellites

The polar orbiting POES constellation operates at an altitude of ~850 km with a ~98.5° inclination. Each satellite transits the Earth ~14 times a day, with an orbital period of ~100 min. As a result of the high-inclination orbit, an L* range spanning from L* < 1.3 to L* > 8.5 can be sampled, dependent on activity, providing a cross section of the radiation belts every ~25 min. Each POES satellite is Sun-synchronous and operates over a limited range of MLT. In this study data from multiple POES spacecrafts have been combined, yielding rapid observations of the radiation belt region across multiple MLT planes, an important consideration for electrons at seed population energies (Allison et al., 2017).

Since the launch of NOAA15, the POES satellites have carried the SEM-2 suite, which includes the MEPED instrument. The MEPED instruments on each satellite were built at the same time and cross-calibrated before being deployed. Furthermore, the instruments undergo a weekly in-flight calibration procedure, detailed in Evans and Greer (2004). As discussed in section 1, MEPED measures integral electron flux data in three energy channels: >30, >100, and >300 keV, all with an upper-energy limit of 2.5 MeV (Evans & Greer, 2004). MEPED contains two solid state detector telescopes, T0 and T90, mounted in perpendicular orientations, both with a ±15° viewing angle. The field-of-view center axis of T0 is rotated 9° from the zenith, while the other telescope, T90, is aligned so that the center of the field of view is 9° from the direction antiparallel to the spacecraft's velocity. The T0 telescope generally samples precipitating electrons in the bounce loss cone (Rodger, Clilverd, et al., 2010) while T90 generally observes a mix of trapped, drift loss cone, and bounce loss cone electrons for much of the radiation belt region (Rodger, Carson, et al., 2010). Following the approach outlined by Rodger, Carson, et al. (2010), we use the International Geomagnetic Reference Field model (Thébault et al., 2015) for mid-2011 to determine the angular width of the loss cone and hence the electron populations sampled by the T90 telescope of MEPED. By considering the ±15° of the telescope, Figure 1 shows the fraction of the T90 telescope field of view that sampled trapped electrons at each location for NOAA15 data from 2011. Due to

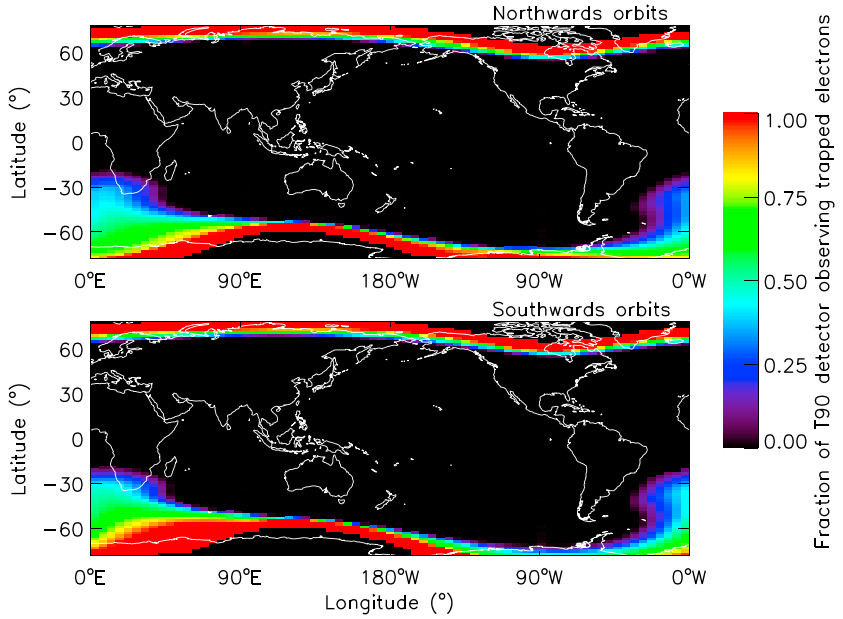

Figure 1. World map showing the fraction of the T90 telescope ±15° viewing angle observing trapped electrons for 2011 NOAA15 data.

significant difference in the pitch angles viewed, highlighted by Rodger, Carson, et al. (2010), northward and southward going orbits have been considered separately.

Rodger, Carson, et al. (2010) suggested that when trapped electrons are observed by T90, this will largely dominate the measurement. Since the directionality is introduced to the measurement by assuming an isotropic incident flux (Yando et al., 2011), if the trapped population is observed for only a fraction of the look direction and largely dominates the reading, this assumption will result in an underestimation of the electron flux. From considering averaged electron flux values, when the T90 detector entirely viewed the trapped electron population, we see that the flux can be approximately a factor of 4 larger than when no trapped electrons are observed. Here we have ignored measurements where less than 20% of the field of view responded to trapped electron flux and used $f_{\text{corrected}} = f_{\text{measured}}/(0.75\tau + 0.25)$ to approximately correct for when only a fraction of the detector, τ, observed the trapped population.

The first POES satellite carrying the SEM-2 detector was NOAA15, launched in 1998, and the last and final POES satellite to be deployed was NOAA19, launched in 2009. The POES series was succeeded by the Meteorological Operational (MetOp) satellites, owned by the European Space Agency and operated by the European Organisation for the Exploitation of Meteorological Satellites (EUMETSAT). To date, two MetOp satellites are currently operational, MetOp-A and MetOp-B, and an additional MetOp satellite (MetOp-C) is still to be launched. The MetOp satellites operate at a similar altitude and orbital inclination to the original POES satellites. Furthermore, for data continuity, MetOp satellites also carry the same SEM-2 instrument as the POES fleet. As a result, the methods described in this paper may also be applied to the MetOp MEPED data. Ultimately, using the described methods on the MetOp data could be used to provide detailed information on the seed population once the Van Allen Probes are no longer operational. For the remainder of the paper no distinction is made between POES and MetOp satellites and the term *POES satellites* may refer to either.

All electron flux values measured by the POES satellites used here have been corrected for ring current protons using the bow tie method described by Lam et al. (2010). During solar energetic proton events, the electron channels of MEPED may be contaminated by proton flux and the electron flux measurements taken during such periods are unlikely to result in representative levels of the seed population. Data collected during solar energetic proton times, defined as when the level of the >10-MeV proton flux measured by the Energetic Particle Sensor on board the Geostationary Operational Environmental Satellites (GOES) 10 and GOES 13 exceeded 10 $cm^{-2}{\cdot}s^{-1}{\cdot}sr^{-1}$, were omitted from the study. The L* values for the POES data used in this study have been calculated using International Geomagnetic Reference Field and the T96 external field (Tsyganenko, 1995).

3. Convert to Omnidirectional Flux

The electron flux at a particular time and location in the magnetosphere typically depends on both energy and pitch angle (Gannon et al., 2007; Horne et al., 2003; Ni et al., 2015; Shi et al., 2016). We have assumed that the integral flux is conserved along the field line, so the local ~90° flux measured by the POES satellites at low Earth orbit are therefore equivalent to the flux of electrons at a smaller equatorial pitch angle given by conservation of the first adiabatic invariant. In effect, we have assumed that the POES integral flux measurement can be mapped down the field line to describe the electron flux at a small equatorial pitch angle. Following this, the omnidirectional flux can then be calculated from the POES measurement by considering an appropriate equatorial pitch angle distribution and integrating over all pitch angles. This is required particularly for the integral to differential flux conversion using the AE9 model flux energy distributions, detailed in the following section, as the AE9 model returns omnidirectional flux (Ginet et al., 2013).

Previous work has sometimes assumed that the electron flux, j, at energy, E, has a pitch angle distribution of $j(E,\alpha) = j(E,90°)\sin^{n(E)}\alpha$ (Gannon et al., 2007; Vampola, 1997). Typically, as electron flux distributions generally decrease with increasing energy (Cayton et al., 1989), integral flux measurements are dominated by electrons with energies just above the lower cutoff. Assuming that at a particular location $n(E)$ changes relatively slowly with energy in comparison to the decrease in electron flux, then for the electron energies that dominate the integral flux measurement, $n(E)$ is relatively constant. Hence, we have assumed that the integral electron flux greater than energy threshold E_T at equatorial pitch angle α can be approximated by

$$F(E>E_T,\alpha) = F(E>E_T,90°)\sin^{N(E_T)}\alpha. \tag{1}$$

where the energy-dependent $n(E)$ parameter has been replaced with $N(E_T)$, a shape parameter for the integral flux that depends instead on the lower-energy threshold, E_T. The variable $F(E>E_T, 90°)$ is the integral flux of electrons with energies greater than E_T at an equatorial pitch angle of 90°. By integrating equation (1) over all solid angle, the omnidirectional integral electron flux can be obtained:

$$F(E>E_T) = 2\pi F(E>E_T,90°)\int_0^{\pi}\sin^{N(E_T)+1}\alpha\,\mathrm{d}\alpha. \tag{2}$$

Evaluating the integral of equation (2) and substituting in equation (1) for $F(E>E_T, 90°)$ we obtain an expression for the omnidirectional integral flux of electrons with energies greater than E_T, given the integral flux measurement at pitch angle α

$$F(E>E_T) = 2\pi\frac{F(E>E_T,\alpha)}{\sin^{N(E_T)}\alpha}\frac{\sqrt{\pi}\Gamma(1+\frac{N(E_T)}{2})}{\Gamma(\frac{3+N(E_T)}{2})} \tag{3}$$

where Γ refers to the gamma function.

The MEPED instrument on board the POES satellites supplies >30-, >100-, and >300-keV electron flux measurements. To convert each of these three flux readings to omnidirectional flux using equation (3), the parameters N(>30 keV), N(>100 keV), and N(>300 keV) were required. Shi et al. (2016) had previously found the $n(E)$ values for the differential flux of electrons with energies varying from 100 keV to 1 MeV using MagEIS data. We instead require $N(E_T)$ values to describe the pitch angle distributions of the integral flux measured by the electron channels of the MEPED detector. The level 3 data from the MagEIS instruments onboard the Van Allen Probes provide high-resolution electron flux measurements over the energy range ~30 keV to 4 MeV, in 11 pitch angle bins. For each pitch angle bin, we interpolated the MagEIS data to the lower-energy threshold of each POES electron channel. The MagEIS electron flux measurements between the lower-threshold energy and 2.5 MeV were then integrated to provide the >30-, >100-, and >300-keV electron flux for each pitch angle bin. The centroid of the pitch angle bins were mapped to the equator to give the equatorial pitch angle of the MagEIS integral flux.

Background-corrected MagEIS data from 1 January 2013 till 31 May 2016 were used to calculate the >30-, >100-, and >300-keV flux for a range of equatorial pitch angles. The integral flux data were sorted into bins of width 0.2L* with centroids between L* = 1.5 and 5.7, by equatorial pitch angle with a resolution of 2°, and by three levels of activity defined by the Kp index (Kp < 2, 2 ≤ Kp < 4, and Kp ≥ 4). The parameter L* for the MagEIS data was calculated using the International Geomagnetic Reference Field and the T89 external field

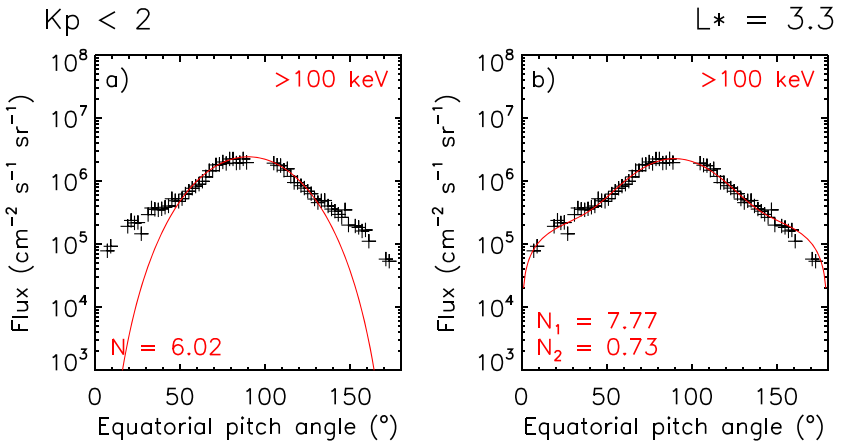

Figure 2. A comparison of (a) fitting equation (1) (red line) to the Magnetic Election Ion Spectrometer >100-keV pitch angle distribution at L* = 3.3, Kp < 2 (black plus symbols) and (b) instead fitting equation (4) (red line).

(Tsyganenko, 1989). For each bin that contained more than 20 values, the mean was evaluated, giving the average equatorial pitch angle distribution of the electron flux for each activity and L*. Equation (1) was then fitted to the data using a nonlinear least squares fit.

At L* values that generally relate to the outer edge of the inner belt, equation (1) did not always provide a good fit to the observations. Figure 2a shows how the average >100-keV flux (Kp < 2 and L* = 3.3 bin) changes with equatorial pitch angle (black plus symbols). Overplotted is the result of fitting equation (1) to the data (red line). It is clear that for pitch angles away from 90°, the fit may significantly underestimate the electron flux. For some activities and L* values we instead assume the following form for the equatorial pitch angle distribution:

$$F(E > E_T, \alpha) = A_0 F(E > E_T, 90°) \sin^{N_1(E_T)} \alpha + (1 - A_0) F(E > E_T, 90°) \sin^{N_2(E_T)} \alpha \quad (4)$$

where A_0 is a parameter in the range $0 < A_0 \leq 1$ and we have two shape parameters, $N_1(E_T)$ and $N_2(E_T)$. Figure 2b shows the result of applying this new distribution to the average >100-keV data. For $\alpha \leq 20°$ and $\alpha \geq 160°$ the fit is now closer to the observations, having reduced the difference by an order of magnitude or more.

The shape of the pitch angle distribution shown in Figure 2 is most likely due to the effect of hiss waves on the electrons. Lyons et al. (1972) showed that within the slot region, the pitch angle diffusion coefficient can show a minimum with respect to pitch angle as regions of significant diffusion by cyclotron resonances and by the Landau resonance are separated in pitch angle. In the slot region, Meredith et al. (2009) also showed similar deep minima in the pitch angle diffusion coefficients calculated by the PADIE code (Pitch Angle and energy Diffusion of Ions and Electrons; Glauert & Horne, 2005), using wave observations from two satellites. A significant reduction in the total diffusion rate for pitch angles between the effective range of the Landau and cyclotron resonances results in hiss waves primarily scattering electrons with pitch angles away from 90°. The population near 90° is scattered at a much slower rate, producing an equatorial pitch angle distribution that is mostly flat, with a sharp peak around 90°. Zhao et al. (2014a) has previously presented observations of the pitch angle distributions of 460-keV differential electron flux that showed a similar form to those seen in Figure 2. They referred to these pitch angle distributions as having a *cap* form.

Examples of the average equatorial pitch angle distributions derived from MagEIS data for two L* bins, L* = 3.1 and L* = 4.9, are shown in Figure 3. Depending on which best suited the observations, either equation (1) or (4) was fitted to the data. For all activity levels and energies in the L* = 3.1 bin, equation (4) was fitted to the data. For L* = 4.9, equation (1) was fitted to the data. The *N* shape parameters for each fit are given in the bottom left-hand corner of each panel. When the single sine function was appropriate, these values can be used in equation (3) with the POES observations to give the omnidirectional flux. For pitch angle distributions where equation (4) was instead fitted to the MagEIS data, the omnidirectional flux is given by

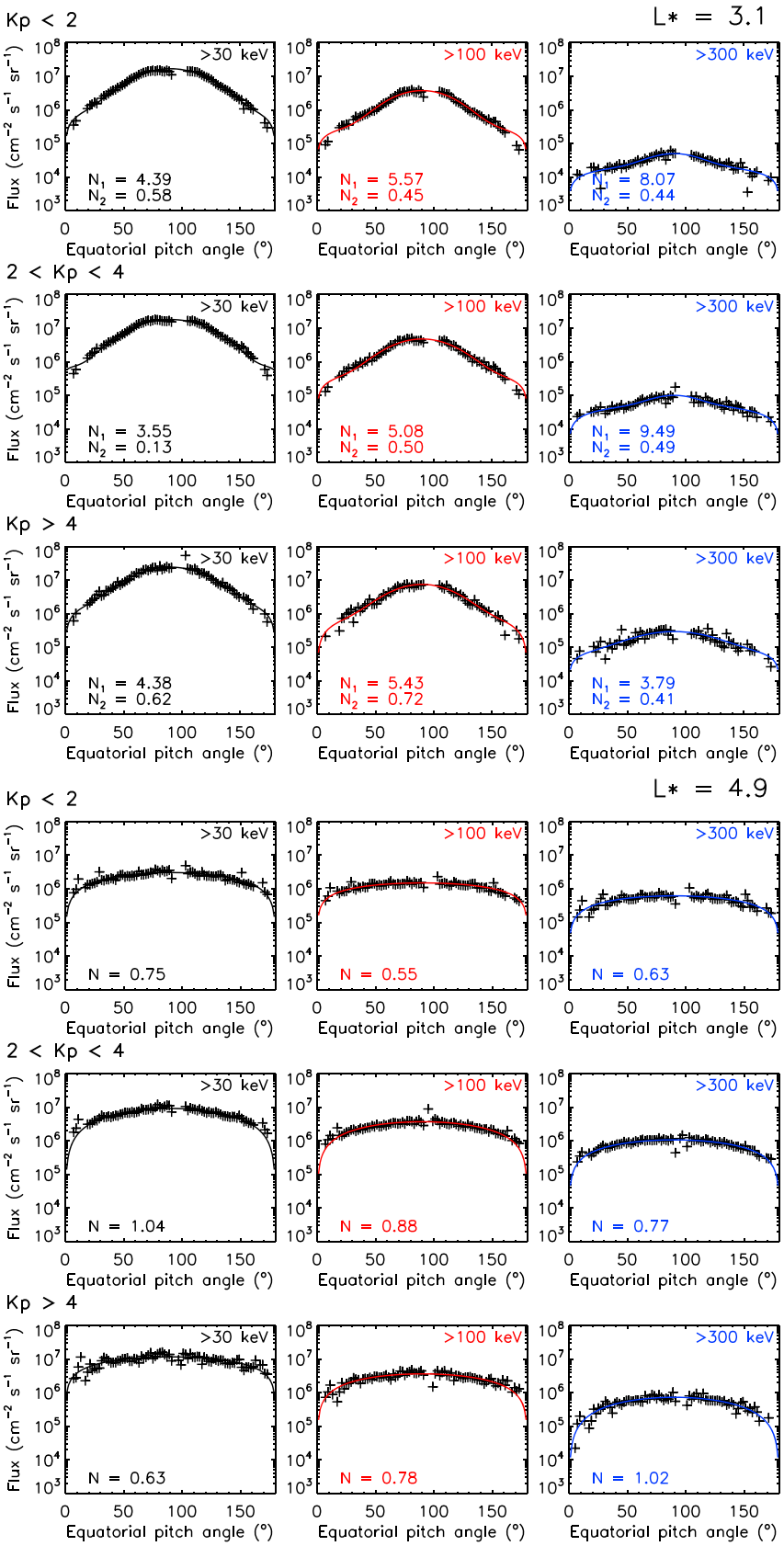

Figure 3. Examples of fitting either equation (1) or (4) to the Magnetic Election Ion Spectrometer data (black plus symbols) for L* = 3.1 and L* = 4.9.

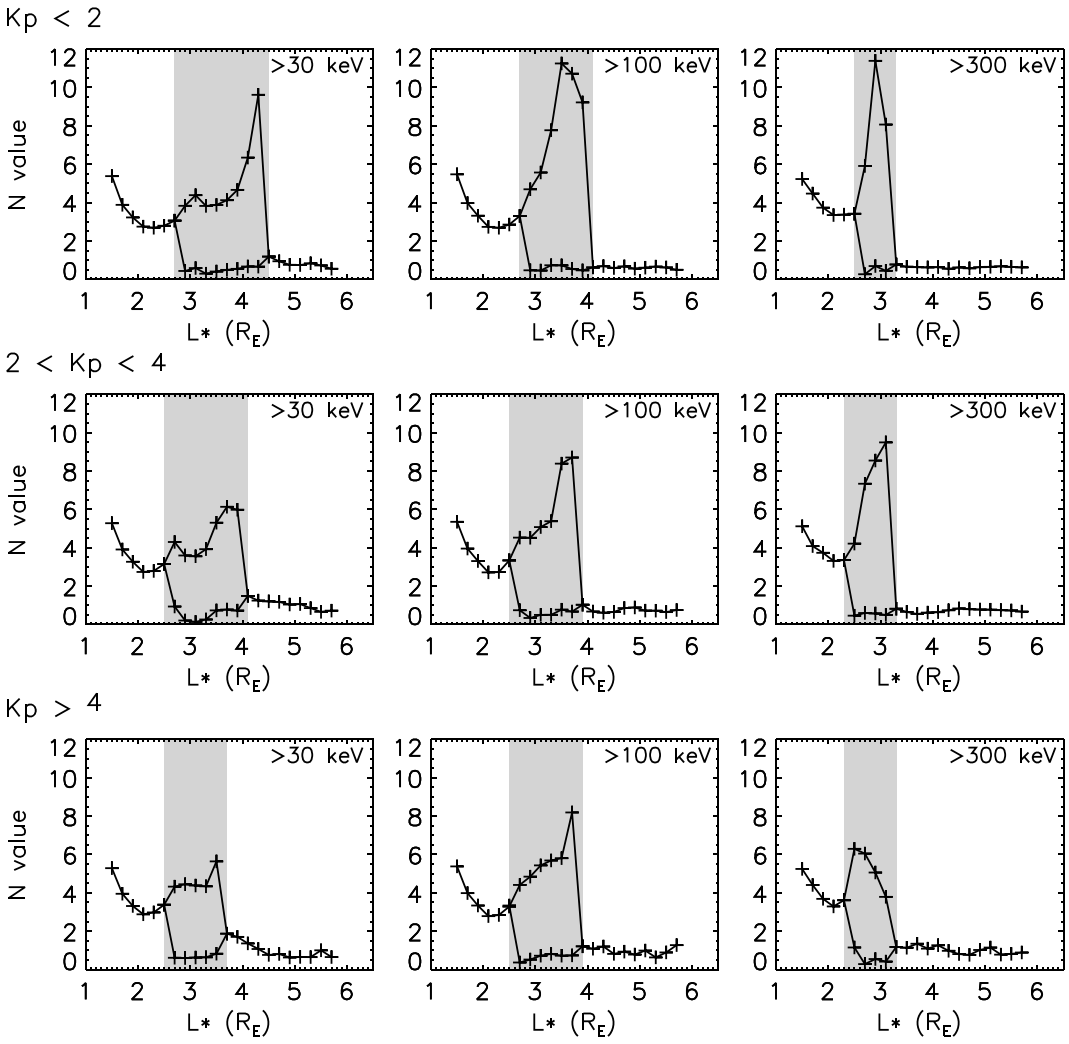

Figure 4. *N* value parameters found from Van Allen Probes measurements across a range of L* values for >30-, >100-, and >300-keV electrons at three levels of Kp. L* values where equation (4) was used in place of equation (1) are shaped in gray.

$$F(E > E_0) = 2\pi F(E > E_0, 90^o)\left(A_0 \frac{\sqrt{\pi}\Gamma(\frac{N_1(E_0)}{2} + 1)}{\Gamma(\frac{3+N_1(E_0)}{2})} + (1 - A_0)\frac{\sqrt{\pi}\Gamma(\frac{N_2(E_0)}{2} + 1)}{\Gamma(\frac{3+N_2(E_0)}{2})}\right) \quad (5)$$

where all parameters are as previously defined and $F(E > E_0,90°)$ can be found from equation (4).

The *N* values obtained by fitting equation (1) to the average pitch angle distributions for >30-, >100-, >300-keV electrons are plotted against L* in Figure 4. The gray regions highlight L* values where the double $\sin^N \alpha$ distribution (equation (4)) was used for the fitting in place of equation (1) and, for these L* values, the two resulting *N* values are instead plotted. The $N(E_T)$ values decrease with L* for L* ≤ 2.5, then follow a form best described using equation (4) out to L* ~ 4, and finally flatten out at $N \sim 0.5$. The last L* bin shown in Figure 4 is L* = 5.7. While MagEIS data was available at larger L*, there were fewer flux measurements for these L* values, particularly for Kp > 4. For this reason we did not use the MagEIS data to calculate the $N(E_T)$ values for L* > 5.7. However, as the $N(E_T)$ values showed little variation with L* beyond L* ~ 5, one might expect the $N(E_T)$ parameters to also remain at a similar level for larger L*.

By using either equation (3) or (5) and the $N(E_T)$ values given in Figure 4 the POES integral flux measurements taken at low Earth orbit, mapped to small equatorial pitch angles, were converted to omnidirectional flux.

4. Integral to Differential Flux Conversion

Previous work has made use of a variety of methods to infer the differential flux from integral measurements. Singular Value Decomposition (Höcker & Kartvelishvili, 1996) was used to calculate particle flux at a high-energy resolution from the integral count rates measured by the Standard Radiation Environment Monitor (Sandberg et al., 2012). As part of a technique to remove proton contamination from the electron channels of MEPED, an inversion method was used to estimate the differential electron flux of the precipitating POES data (T0 detector; Peck et al., 2015). The spectral shape used in the method presented by Peck et al. (2015) was calculated using a combination of exponential, power law, single relativistic Maxwellian, and a double relativistic Maxwellian. In addition, past work has also used integral flux to derive boundary conditions for radiation belt models. GOES integral electron flux data were used to formulate boundary conditions for the VERB-3D radiation belt model in order to study the September 2012 storm (Shprits et al., 2013). Here we present two novel methods to convert from integral electron flux to differential flux across a range of energies, with focus on 100- to 600-keV electrons.

4.1. Method One: Using Distributions From the AE9 Model

AE9 is a recently developed standard design model of radiation belt flux levels for the purposes of spacecraft engineering. The development and features of AE9 are detailed by Ginet et al. (2013). The AE9 model was formed using measurements made by particle detectors onboard 33 satellites in a variety of orbits, comprehensively cross-calibrated. By making use of this extensive database, AE9 is capable of returning the omnidirectional electron flux energy profile averaged over a chosen orbit, giving both integral and differential flux, making it a powerful tool for spacecraft design. The electron flux corresponding to various percentiles, ranging from the 2nd to the 98th, can be selected.

Using version 1.3 of the AE9 model, we extracted the distribution of omnidirectional integral flux against lower-threshold energy and the profile of omnidirectional differential flux against energy for percentiles ranging from the 2nd to the 98th, at each radii considered. Circular orbits at the equator were used, with radii ranging from 1.5 R_E to 8 R_E in steps of 0.25 R_E. An example of both the integral and differential flux distributions at a distance of 4 R_E are shown in Figures 5a and 5b respectively; various colors relate to different percentiles. Panels c and d show the AE9 model flux energy profiles relating to the 50th percentile of the integral and differential flux for orbits of varying radii.

In the geomagnetic field, the L* parameter does not directly relate to a radial distance at the magnetic equator. However, we assume that the flux energy profile for a particular L* value may be largely described by one of the distributions averaged over a circular orbit with a radius R in the range $(L^* - 1) \leq R\,(R_E) \leq (L^* + 1)$. For each POES electron flux measurement, we found AE9 average flux profiles relating to 9 distances in the $(L^*\text{-}1) \leq R\,(R_E) \leq (L^*\text{+}1)$ range, at intervals of 0.25 R_E. For each of the resulting nine circular orbits, a flux energy distribution was given for each integer percentile value spanning from the 2nd to the 98th. The omnidirectional >100-keV POES flux value was then compared to the >100-keV AE9 flux values to find the percentile at each of the nine distances closest to the >100-keV observation. The percentiles with values for the >100-keV flux that lay immediately either side of the POES observation were interpolated to give an integral flux energy distribution that passed through the omnidirectional value of the >100-keV POES flux. The same scaling was also applied to the equivalent differential flux distributions.

After comparing the >100-keV flux to the various AE9 flux energy profiles, we are left with nine integral flux energy distributions, each passing through the POES value of the omnidirectional >100-keV flux and nine corresponding differential flux distributions. Each integral and differential flux energy distribution pair relates to one of the distances in the specified range. By comparing the >300-keV omnidirectional flux obtained from the POES satellite measurement to the >300-keV flux from the remaining integral flux profiles, we identified the AE9 distribution closest to observations. This integral flux distribution was extracted, as was the corresponding differential flux profile. For integral flux values with a lower-threshold energy greater than 300 keV, a scaling factor was applied to the final integral flux distribution so that the >300-keV flux passed through the observed value. The same scaling factor was applied to the extracted differential flux distribution for energies greater than 300 keV.

The final differential flux profile was assumed to describe the flux energy distribution at the POES measurement time. Repeating the above process for all times where the POES satellite observed trapped flux returned

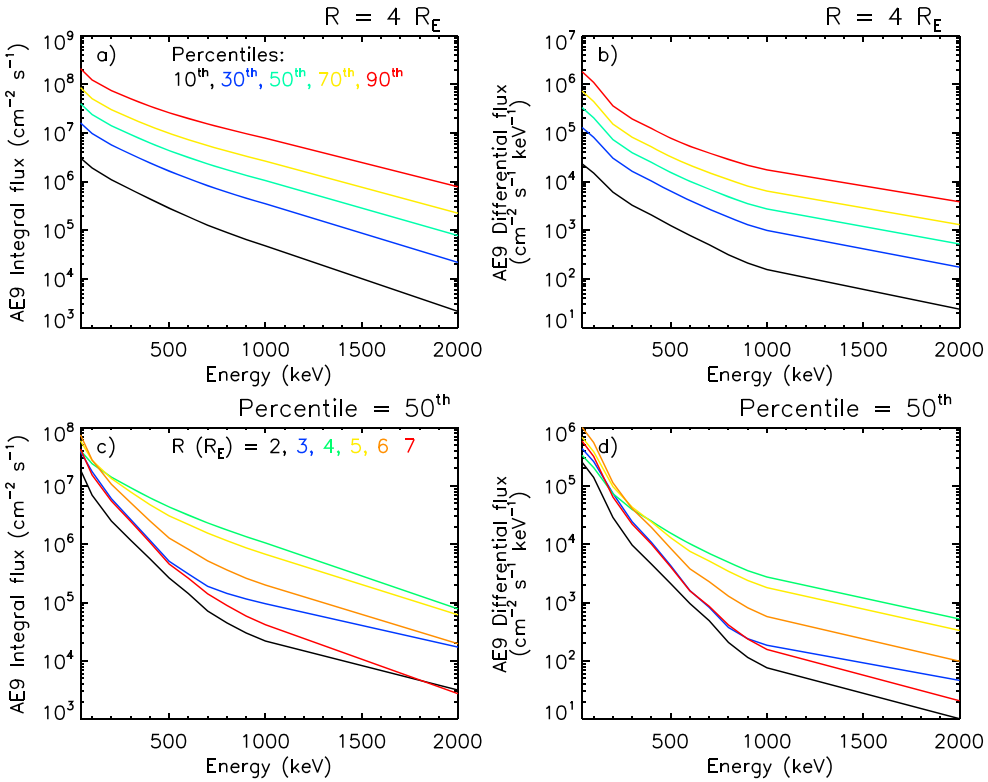

Figure 5. Flux energy distributions from the AE9 model. The integral electron flux against the lower-energy threshold (a) and differential flux against energy (b) are shown for a circular satellite orbit at the magnetic equator with a radius of 4 R_E. For panels (a) and (b) the black line shows the AE9 data equating to the 10th percentile, blue shows the 30th percentile, green shows the 50th, yellow the 70th, and red the 90th. The integral (c) and differential flux (d) relating to the 50th percentile are shown for circular orbits of various radii. In panels (c) and (d) the black line shows the AE9 data for an orbit radius of 2 R_E, blue for 3 R_E, green for 4 R_E, yellow for 5 R_E, orange for 6 R_E, and red for 7 R_E.

an estimate of the omnidirectional differential flux for the period. The energy values for the differential electron flux equate to the energies requested from AE9 model, which can be as low as 40 keV.

4.2. Method Two: Using an Iterative Fit

Using the integral flux values, we applied an iterative approach, based on a RMC method (McGreevy & Pusztai, 1988), to recreate the differential flux distribution. The iterative method employs a simple basic process. An initial flux energy distribution was set and χ^2 calculated:

$$\chi^2 = \sum_{n=1}^{3} \frac{(\log_{10}(f_{calc}(E > E_n)) - \log_{10}(f_{obs}(E > E_n)))^2}{\sigma_{err}^2} \quad (6)$$

where $f_{calc}(E > E_n)$ defines the integral flux values calculated from the initial flux energy distribution for >30-, >100-, and >300-keV electrons and $f_{obs}(E > E_n)$ are the corresponding POES observations. As the flux at different energies may vary by several orders of magnitude, we perform the iterative calculation in log space. The parameter σ_{err} is the error margin on the logarithm of the observed integral flux measurements. One of the flux values in the flux energy distribution was then randomly selected and the logarithm of the flux moved up or down by a random value of up to 0.1. Following the move, χ^2 was recalculated, and if the value was smaller than the previous χ^2, the move was accepted. If the new χ^2 was larger than the previous value then the move was accepted with a probability following the normal distribution. The process was repeated iteratively, and the outcome is a differential flux energy distribution which, when integrated, should reproduce the POES measurements to within the error margin.

Several distribution shapes may return the observed integral flux values. Ideally, we require additional measurements to direct the result toward the actual distribution. In the absence of extra measurements, we applied the constraint that the flux must fall with increasing energy. This assumption was also made in section

3 and is generally reasonable as electron flux distributions typically decrease with energy (Cayton et al., 1989). The energy spacing between flux values should be constant so that during the random selection stage, the flux at each energy has an equal probability of being selected. To avoid having too many flux values, which would act to slow the iterative progression down, while still retaining a fine energy resolution at the seed population energies of interest, we assumed that above 1.2 MeV, the electron flux contributed little to the integral flux measurements and could be negated without considerable impact to the result. Following this, we then considered the integral flux values to have an upper-energy threshold of 1.2 MeV instead of the 2.5 MeV of the POES electron channels (Evans & Greer, 2004).

Initially, 118 flux values were set for energies ranging from 30 keV to 1.2 MeV, obeying the following form

for 30 keV $\leq$ E < 600 keV:

$$\log_{10}(f(E)) = A - \frac{(A-B)(E-30)}{(600-30)} \tag{7}$$

for 600 keV $\leq$ E < 1.2 MeV:

$$\log_{10}(f(E)) = B - \frac{(B-C)(E-600)}{(1200-600)} \tag{8}$$

where $f(E)$ is the omnidirectional electron differential flux, E the electron energy in keV, $A = \log_{10}(f(30\text{ keV}))$, $B = \log_{10}(f(600\text{ keV}))$, and $C = \log_{10}(f(1.2\text{ MeV}))$. The electron flux at 30 keV was estimated using the POES >30- and >100-keV measurements, assuming a constant flux between 30 and 100 keV. Likewise, the electron flux at 600 keV was estimated using the POES >300-keV measurement by assuming a constant flux from 300 keV to 1.2 MeV. As the electron flux at 1.2 MeV is likely significantly lower than the flux at 600 keV, we subtract 1.5 from the logarithm of the estimated 600-keV flux as a first estimate for C. The distribution resulting from equations (7) and (8) was then used as the initial flux energy profile in the iterative RMC style method.

For the χ^2 calculation given by equation (6) we required a value for σ_{err}, the error value on the logarithm of the omnidirectional POES flux measurement. Sources of error include uncertainties in the instrument correction factors, Poisson noise in the count data, as well as errors incurred from the bow tie correction (Lam et al., 2010). Further errors are also introduced when converting to omnidirectional flux: by the pitch angle distributions assumed and the parameterization by Kp. Considering the above, we adopted a 40% error in the POES measurement values, which yields a σ_{err} of approximately 0.2. It should be noted that assuming a larger measurement error of 50% (where σ_{err} ~0.24) did not notably impact the resulting spectra.

The described iterative method was applied to POES omnidirectional integral electron flux data for each measurement time. The result was an estimate of the omnidirectional differential flux, at energies between 30 keV and 1.2 MeV in 10-keV increments.

5. Conversion to 90° Electron Flux

Following the application of one of the methods described in section 4.1 or 4.2, the POES electron flux data have been used to estimate the omnidirectional electron flux at a number of energy values. As a final step, the omnidirectional electron flux was converted back to directional flux by assuming a pitch angle distribution at each energy, E, that obeys either a

$$j(E,\alpha) = j(E,90^\circ)\sin^{n(E)}\alpha \tag{9}$$

or

$$j(E,\alpha) = A_0 j(E,90^\circ)\sin^{n_1(E)}\alpha + (1-A_0)j(E,90^\circ)\sin^{n_2(E)}\alpha \tag{10}$$

distribution in pitch angle. The shape parameter, $n(E)$, for the pitch angle distribution of differential flux (as opposed to $N(E_T)$ for integral flux) is dependent on both the electron energy and the L* of the measurement.

Shi et al. (2016) had previously evaluated the $n(E)$ shape parameters for differential electron flux using the level 3 MagEIS data and assuming the distribution given by equation (9). Here we have binned the electron flux data

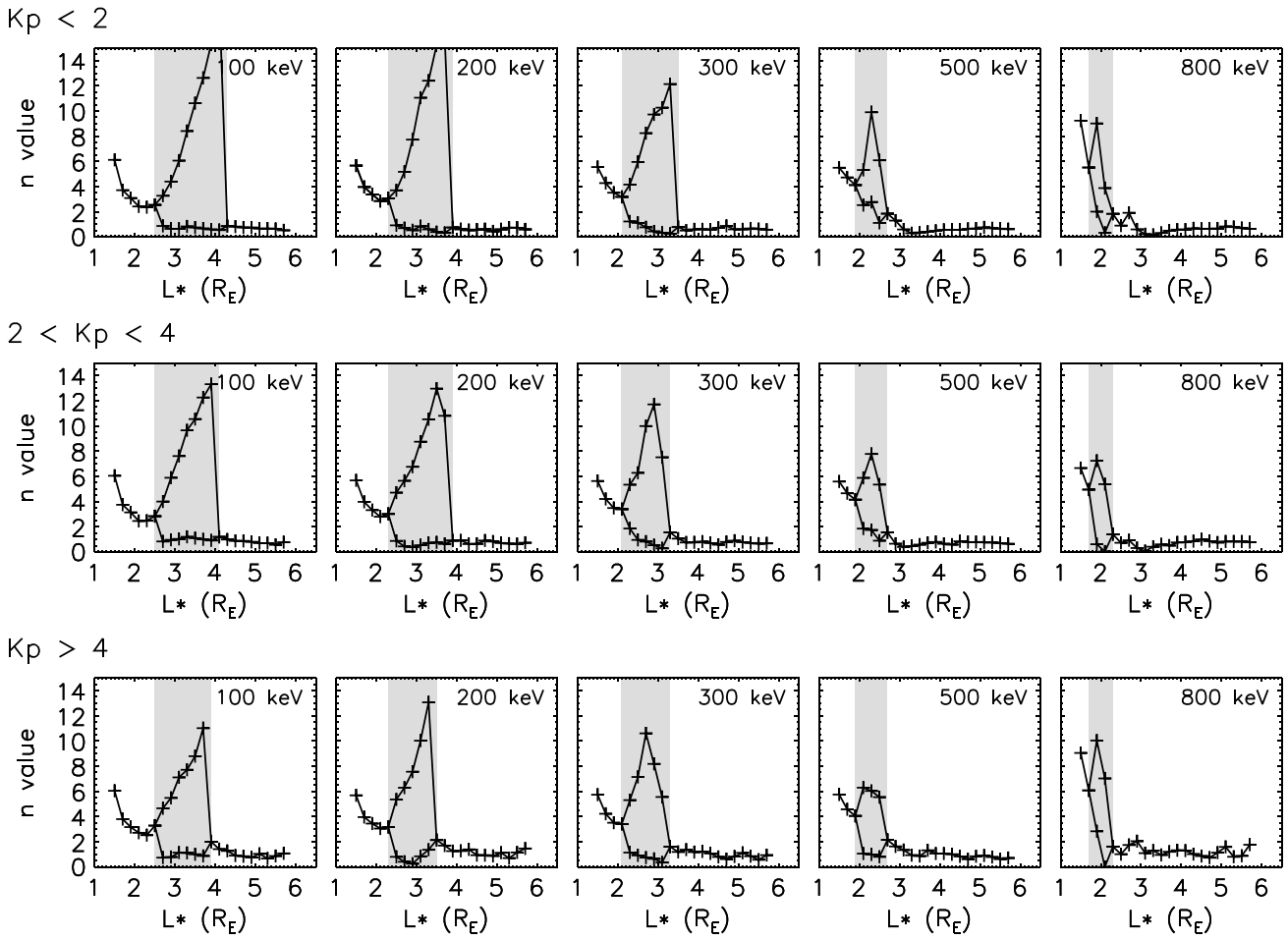

Figure 6. The $n(E)$ value shape parameters found from Magnetic Election Ion Spectrometer differential flux measurements across a range of L* values for 100-, 200-, 300-, 500-, and 800-keV electrons at three levels of Kp. L* values, where a double sine function was fitted instead of a single sine function, are shaped in gray.

by L* instead of the L used by Shi et al. (2016), making the conversion to directional flux consistent with the rest of the study. Additionally, when considering integral flux, we identified that a single sine distribution was not always an appropriate fit to the data (Figure 2). This was mirrored by the differential flux equatorial pitch angle distributions, again for L* values relating to the outer edge of the inner belt. Zhao et al. (2014a) also found differential flux pitch distributions with a sharp peak near 90°, referred to as cap pitch angle distributions in their study. In this work we build on the study by Shi et al. (2016) by forming L*-dependent $n(E)$ values and fitting equation (10), a double sine function, when the single sine form did not offer a good fit to the data.

Background-corrected level 3 MagEIS data were interpolated to 100, 200, 300, 500, and 800 keV, then, as in section 3, binned by Kp, L*, and equatorial pitch angle. The binned data were averaged to form statistical equatorial pitch angle distributions for the differential flux at the listed five energies, for L* bins with centroids ranging from L* = 1.5 to 5.7 in steps of 0.2L*, and at three levels of the activity index Kp. A single or double sine distribution was then fitted to the average distributions to determine appropriate $n(E)$ parameters for each L* bin, energy, and activity level.

By integrating equation (9) over all solid angle we obtain an expression similar to equation (3), and rearranging for the 90° electron flux gives

$$j(E,90^\circ) = \frac{j(E)}{2\pi}\frac{\Gamma(\frac{3+n(E)}{2})}{\sqrt{\pi}\Gamma(1+\frac{n(E)}{2})} \tag{11}$$

where, as in equation (3), Γ denotes the gamma function. Likewise, integrating equation (10) gives the following expression for the differential flux of 90° electrons:

$$j(E,90^\circ) = \frac{j(E)}{2\pi}\left[A_0\frac{\sqrt{\pi}\Gamma(1+\frac{n_1(E)}{2})}{\Gamma(\frac{3+n_1(E)}{2})} + (1-A_0)\frac{\sqrt{\pi}\Gamma(1+\frac{n_2(E)}{2})}{\Gamma(\frac{3+n_2(E)}{2})}\right]^{-1} \quad (12)$$

The $n(E)$ values found from fitting either equation (9) or (10) to the average pitch angle distribution for differential flux are shown in Figure 6. The gray regions show where equation (10) has been fitted. For 100- and 200-keV electrons, in particular, the n_1 values obtained from fitting equation (10) to the pitch angle distribution rose continually with increasing L*. The rise in n_1 was paired with a reduction in the A_0 parameter with increasing L* (not shown). This implies that as the peak around 90° narrowed with increasing L* the height reduced. Eventually, the peak around 90° became indistinguishable from the rest of the pitch angle distribution, and a single sine form was again appropriate. The $n(E)$ values shown in Figure 6 were used in accordance with equation (11) or (12) to determine the electron flux energy distribution at an equatorial pitch angle of 90°. Note that, with a slight alteration, equations (11) and (12) may also be used to convert the omnidirectional flux to equatorial pitch angles other than 90°, although for simplicity, only the results achieved for equatorial pitch angles of 90° are compared to Van Allen Probes data in the following validation section.

6. Validation

To test the methods presented in the previous sections, we compared the differential 90° flux obtained from POES data to background-corrected electron flux measurements from the MagEIS instruments onboard Van Allen Probe A. The Van Allen Probes operate near the magnetic equatorial plane, providing observations of the radiation belts. Figure 7 shows the measured 90° pitch angle electron flux for the month of June in 2013 from eight MagEIS energy channels, ranging between 54 and 742 keV. Data from Probe A were sorted into three L* bins centered on L* = 5.5, 4.5, and 3.5, each of width L* = 0.1. For reference, both the AE and Kp indices are also shown in the bottom panel of Figure 7. It is worth noting that although the Van Allen Probes operate near the magnetic equator, the 90° local pitch angle channel may not always relate to a 90° equatorial pitch angle. However, for the purpose of the following comparison, equivalence is assumed as differences are likely to be minor.

For several periods during June 2013, the electron flux at higher energies exceeded that at lower energies and the flux energy distribution displayed a region of positive gradient. If the measured flux from two consecutive MagEIS energy channels showed an increase with energy, then Figure 7 was shaded in gray. Reeves et al. (2016) first observed a minimum in flux as a function of energy, seen during March 2013, at the inner edge of the outer radiation belt. At this location, electron flux distributions showed a minimum at energies of a few hundred kiloelectronvolts during quiet time conditions. Occurrences of the so-called *S-shaped* energy structure of the outer radiation belt have since been attributed to the combination of radial transport and wave-particle interactions with plasmaspheric hiss (Ripoll et al., 2016, 2017). Figure 7 shows that the 593- and 742-keV electron flux exceed the flux of lower-energy electrons at all three L* values shown, but most commonly at L* = 4.5. In agreement with the findings of Reeves et al. (2016), this typically occurred during quiet periods.

Flux energy distributions that do not fall with increasing energy violate the assumptions made in sections 3 and 4.2. Additionally, electron flux distributions that display a minimum around several hundred kiloelectronvolts are not returned by the AE9 model and so cannot be obtained from the method presented in section 4.1. As a result, during periods when the S-shaped energy structure of the outer radiation belt arises, we would not expect either method presented in this paper to produce realistic 90° differential electron flux. We therefore have omitted these periods from the validation. The issue of the outer radiation belt S-shaped energy structure is discussed further in the following section.

To compare the output of either method 1 or method 2 to the electron flux level observed by Van Allen Probe A, we have produced the scatter plots shown in Figure 8. Six months of data from 2013, ranging from 1 April to 30 September, covering the entire summer season has been used for the validation. During the 6-month period, four POES satellites and one MetOp satellite were operational: NOAA15, NOAA16, NOAA18, NOAA19, and METOP02. The integral electron flux data from each of these satellites was converted into differential

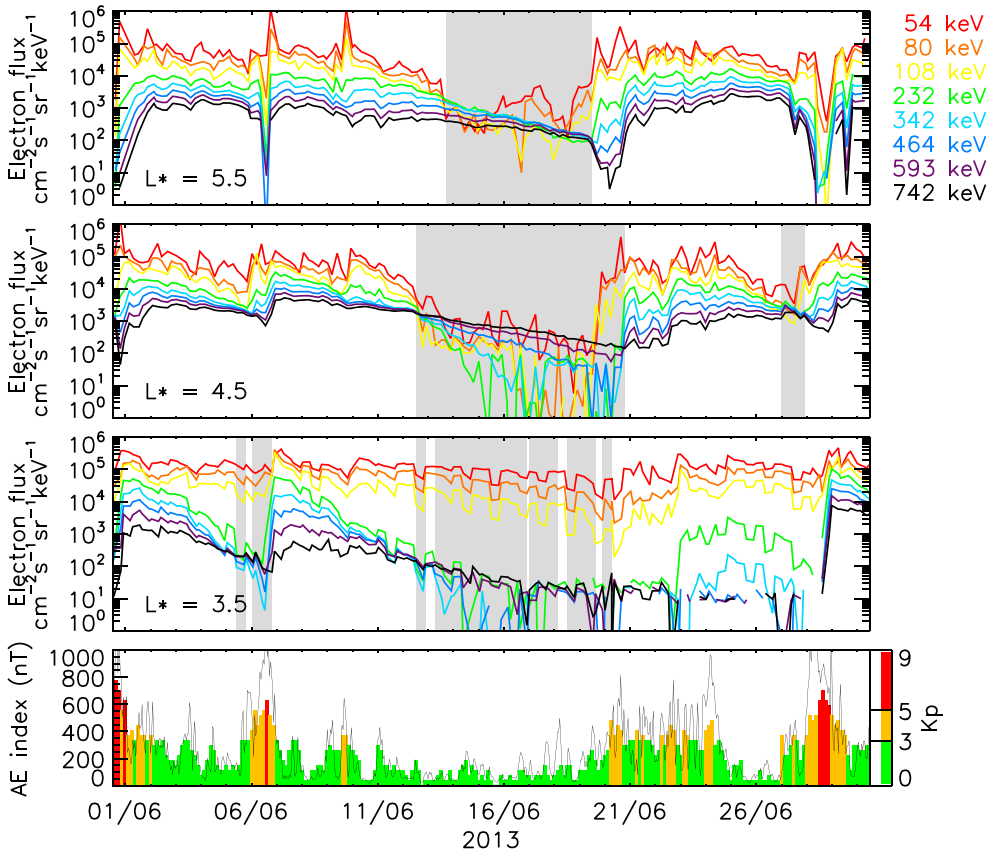

Figure 7. Electron flux measured by the Van Allen Probes during June 2013 for L* = 5.5, 4.5, and 3.5. The Kp and AE index for the period is also shown. Grayed sections indicate where the flux of higher-energy electrons has exceeded that of lower-energy electrons.

flux, then sorted into six L* bins centered on L* = 5.5, 5.0, 4.5, 4.0, 3.5, and 3.0, each of width L* = 0.1. Van Allen Probe A data shown in Figure 7 was sorted by L* in the same manner. For each L* value, the resulting differential flux from the five POES satellites were interleaved, providing the electron flux along an L* cut at a much higher high time resolution than can be obtained from the Van Allen Probes. As the intention is to ultimately compare the converted flux value to that observed by the MagEIS instrument, 2-hr averages were produced from the POES flux data and these averages interpolated to the Van Allen Probe data times. The MagEIS energy channels were interpolated to regular energies ranging from 100 to 600 keV in spacings of 100 keV. We then plotted the 90° electron flux derived from the POES data against the MagEIS flux at the same L*, energy, and time, as shown in Figures 8a and 8c, with points color coded by electron energy. Figure 8a compares the flux resulting from method 1 to MagEIS data while Figure 8b compares the flux from method 2.

A perfect recreation of the Van Allen Probes data would produce a straight line with a gradient of 1. Figures 8a and 8b show a clear positive correlation and a spread that is primarily confined within an order of magnitude of the Van Allen Probes observation. However, there is a tendency for the differential 90° flux obtained from POES data, via either method, to be lower than the observed value, particularly for 500- and 600-keV electrons.

To further aid analysis, the average ratios between the Van Allen Probe A MagEIS observations and the 90° electron flux retrieved from POES measurements were calculated for L* values ranging from 3.0 to 5.5. Figure 8c shows these ratios for the 90° electron flux formed by applying method 1 to the POES data. Different colored lines relate to the energies listed in panel a, and a dashed line marks the ratio value of 1. For L* $\gtrapprox$ 3.7, the average ratios resulting from method 1 were less than a factor of 4 for all energies in the 100- to 600-keV range. Additionally, the average ratios remained relatively constant with L* for each electron energy and typically increased with energy. For L* $\lessapprox$ 3.7, larger differences between the MagEIS measurements and the POES method 1 converted flux were observed. The ratios displayed more variability with changing L* and,

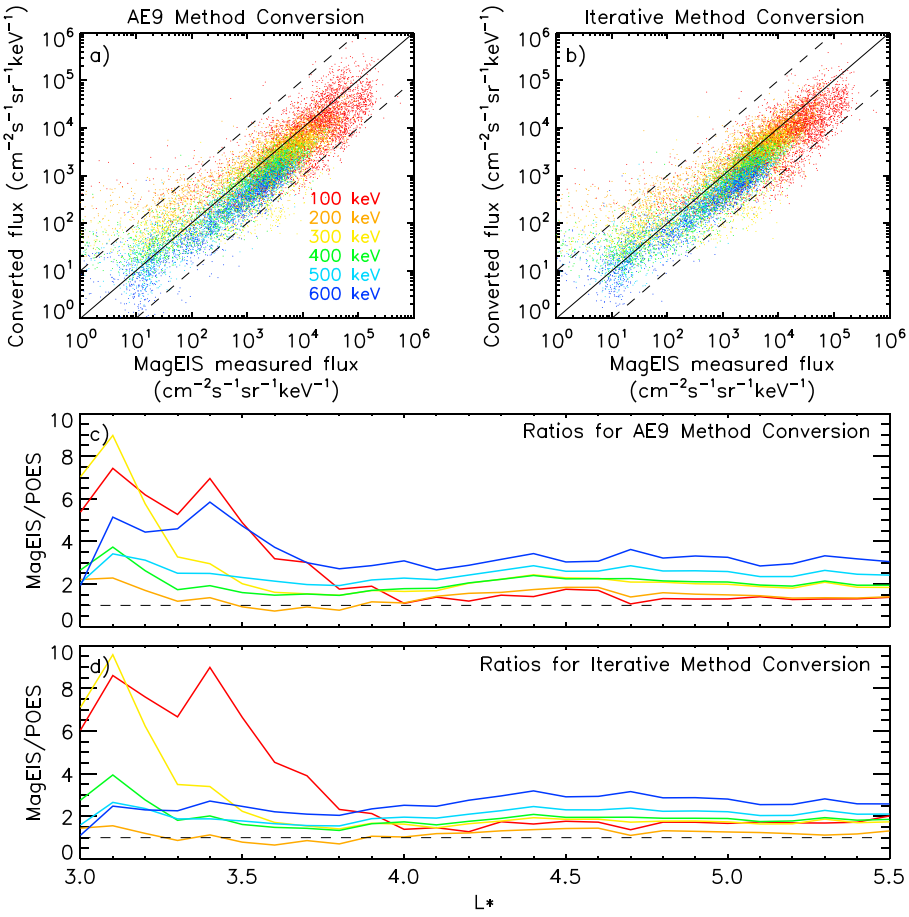

Figure 8. Comparing both conversion methods to Van Allen Probes data. (a) Scatter plot between the electron flux at various energies derived from the Polar Operational Environmental Satellites (POES) data using method 1 and that observed by the Van Allen Probes MagEIS instruments. (b) Same as panel (a) but for POES flux values obtained using method 2. (c) Ratio of MagEIS flux to POES flux values from method 1 for a range of L* values. (d) Same as panel (c) but for method 2. MagEIS = Magnetic Election Ion Spectrometer.

in particular, the difference between the 100-keV MagEIS flux and the 100-keV converted POES flux increased notably. In this L* range, the average ratio values no longer rose with increasing energy.

Figure 8d shows that, generally, differences between the output of methods 1 and 2 were minor. Again for L* $\gtrapprox$ 3.7, the average ratios for the considered energies were less than a factor of 4 and remained fairly consistent with L*. However, a notable variation between methods 1 and 2 is that for L* $\lessapprox$ 3.7 the average ratio values for the 600-keV flux from method 2 (blue line, panel d) are lower than seen for method 1 (blue line, panel c), suggesting the larger ratios for the 600-keV flux from method 1 in this L* range originate from the form of the differential flux spectra assumed using the AE9 distributions. Conversely, the increased ratios for the 100- and 300-keV flux for L* $\lessapprox$ 3.7 are seen in the results of method 2 as well as method 1, indicative that the differences between the POES and MagEIS observations here are unlikely to be a result of the integral to differential flux conversion and may stem from a greater variability in the pitch angle distributions for these energies than has been captured by the three levels of Kp, used in section 5.

In general, Figure 8 illustrates an agreement between the POES converted flux and Van Allen Probes observations that is typically within a factor of 4 for most energy and L* values.

7. Using the POES Data to Form a Low-Energy Boundary Condition

Previous work has shown the importance of a realistic seed population in accurately recreating radiation belt dynamics (Tu et al., 2014). However, in the absence of Van Allen Probes data, the level of the seed population

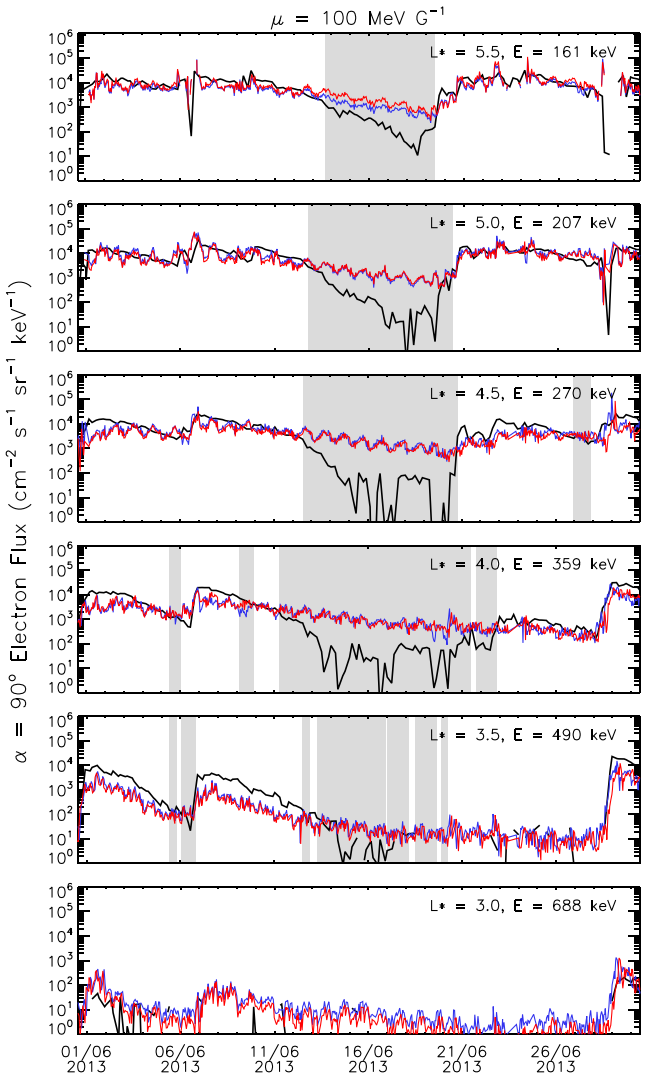

Figure 9. Comparison of the Van Allen Probes Magnetic Election Ion Spectrometer electron flux (black line) at six values of L*, for energies following a line of constant μ = 100 MeV/G and the electron flux outputted by method 1 (red line) and method 2 (blue line). As in Figure 7, grayed regions show periods when the assumption that electron flux falls with increasing energy is violated.

throughout the radiation belt region is generally difficult to ascertain. Here we use the POES data to study the seed population for June 2013 and compare the time sequence of the flux to Van Allen Probe A observations.

Present 3-D radiation belt models generally either set the minimum energy to a constant value throughout the calculation region (e.g., Tu et al., 2013; Wang et al., 2017) or the minimum energy is defined by a line of constant first adiabatic invariant, μ (e.g., Albert et al., 2009; Glauert et al., 2014a). Here we formulate the 90° electron flux at energies following a line of first adiabatic invariant to explore using the presented methods to generate low-energy boundaries for models like the British Antarctic Survey (BAS) Radiation Belt Model (Glauert et al., 2014a). Figure 9 shows both the Van Allen Probe A data (black line) and the output from applying method 1 (red line) and method 2 (blue line) to the POES data, at various L* values covering the outer radiation region. The flux is given for electron energies defined by following a line of μ = 100 MeV/G, calculated assuming a dipole field for simplicity. The value of μ corresponds to an energy of ~161 keV at L* = 5.5 and is therefore a relatively reasonable value for the low-energy boundary of a 3-D Radiation Belt Model for June 2013 (Allison et al., 2017). One hour averages of the converted POES flux are shown. As with Figure 7, periods when more than two energy channels of MagEIS showed that the electron flux did not fall with increasing energy are shaded in gray. It is clear that during these grayed periods, when our underlying assumptions do not hold,

the electron flux obtained from applying either method to the POES data typically overestimates the electron flux. However, for times outside of these gray regions, the converted flux displays a similar shape to the Van Allen Probe data and is mostly within a factor of ~5 of the observations.

In general, throughout the outer radiation belt, we were able to use the POES low Earth orbit integral electron flux measurements to obtain a time sequence for the 90° pitch angle flux at selected seed population energies, which mostly resembled the observations by the MagEIS instruments when the assumption made in both sections 3 and 4.2 held. For smaller L* values, differences between the MagEIS recorded value and the converted POES flux are more apparent; however, general trends in the MagEIS flux variation in time were mostly followed. Flux increases likely associated with the rise in activity on 1, 7, and 29 June are captured in the converted POES flux. Likewise, the sharp decreases in the flux seen at L* = 5.5 and 5.0 on 28 June 2013 are also reproduced. In agreement with the results shown in Figure 8, Figure 9 shows that the two methods return similar results. Thus, it is suggested that using either method described in this paper would provide an adequate realistic low-energy boundary condition.

8. Using the Low-Energy Boundary Condition From POES Data in the BAS Radiation Belt Model

The low-energy boundary condition formulated from POES data for June 2013, shown in section 7, has been used in the BAS Radiation belt model (Glauert et al., 2014a). To avoid starting the simulation during the high-Kp period at the beginning of June 2013 (so electron enhancements are calculated by the model rather than being supplied by the initial condition), we run the BAS Radiation Belt model starting on 3 June 2013. The diffusion coefficients used by Glauert et al. (2018) in the BAS Radiation Belt Model have also been used here. Radial diffusion coefficients are given by the electromagnetic component of the Kp-dependent model from Brautigam and Albert (2000). Pitch angle and energy diffusion coefficients have been calculated by the PADIE code (Glauert & Horne, 2005) and include contributions from whistler mode chorus waves (Horne et al., 2013), electromagnetic ion cyclotron waves (Kersten et al., 2014), plasmaspheric hiss and lightning-generated whistlers (Glauert et al., 2014a). Losses due to magnetopause shadowing are included as described by Glauert et al. (2014b).

The 3-D BAS Radiation Belt Model requires boundary conditions on six surfaces, corresponding to the maximum and minimum of each of the three coordinates: α, energy, and L*. The minimum and maximum α boundaries and the maximum energy boundary condition are defined as described by Glauert et al. (2014a). Van Allen Probes data from MagEIS and Relativistic Electron Proton Telescope have been used to formulate the initial condition and the minimum and maximum L* boundaries. The final low-energy boundary condition has been supplied by POES data following the techniques presented in this study. As performing the conversion from integral flux to differential flux by either method 1 or 2 returns largely similar results in Figure 9, we have used method 1 to generate the low-energy boundary condition for the BAS Radiation Belt Model.

Figure 10b shows the model results for perpendicular 0.9-MeV electrons obtained using the POES low-energy boundary condition. The ~0.9-MeV flux measured by MagEIS is shown in Figure 10a. Both the data and the model output exhibit a small dropout on 6–7 June 2013, during which both the AE and Kp indices increase. Van Allen Probe A then observed an enhanced electron flux which gradually decays over an extended period where Kp remains less than 2. As shown by Figure 7, this quiet period largely encompasses times where *S-shaped* energy structure of the outer radiation belt was observed. The model (Figure 10b) also produces a flux enhancement following the dropout; however, as evidenced by the ratio between the model output and observations in Figure 10d, this flux increase is lower than observed and, for L* > 4, exhibits a slower decay.

A second dropout was observed on 20 June where the AE and Kp indices both increased and remained high for several days. Again, a flux enhancement in both the model output and Van Allen Probe A data was observed following the dropout. In the model output (Figure 10b) this second enhancement extends down to L* = 4, while the observations suggest the flux increase to have been mostly at L* > 4.5. From 22 June, for L* > 4.5, the model-data ratio in Figure 10d suggests a very good agreement between the model and Van Allen probe measurements. Conversely, at lower L*, the disparity in the inward extent of the enhancement produces the model's largest departure from the data.

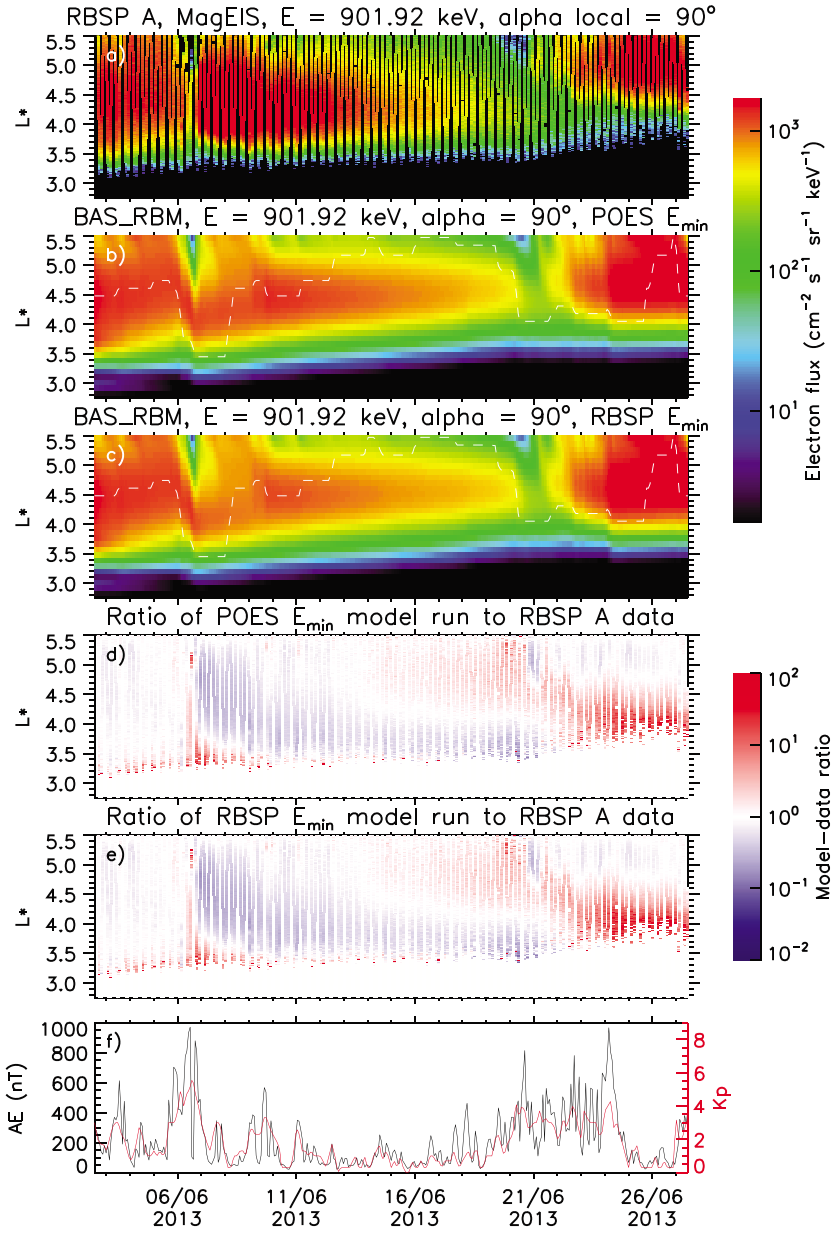

Figure 10. (a) Van Allen Probe A MagEIS flux of 0.9 MeV electrons at a local pitch angle of 90°; (b) 0.9-MeV electron flux from BAS Radiation Belt Model using a low-energy boundary condition supplied by POES data. Dashed white line marks the plasmapause location given by Carpenter and Anderson (1992); (c) same as (b) but using Van Allen Probe A data to supply the low-energy boundary condition; (d) ratio of the 0.9-MeV model flux obtained using the POES low-energy boundary condition to the MagEIS measured values; (e) same as (d) but for the model run using the Van Allen Probes low-energy boundary condition; (f) the Kp and AE indices for the period. MagEIS = Magnetic Election Ion Spectrometer; POES = Polar Operational Environmental Satellites; RBSP = Radiation Belt Storm Probes; BAS-RBM = British Antarctic Survey-Radiation Belt Model.

As a comparison, the results from the BAS Radiation Belt Model, using a low-energy boundary condition formulated from Van Allen Probe A MagEIS data, are shown in Figure 10c. Encouragingly, the model output using the POES low-energy boundary condition (Figure 10b) and the results from using the Van Allen Probes low-energy boundary condition (Figure 10c) are largely similar. This was expected as Figure 9 showed the two low-energy boundary conditions to be fairly alike, generally showing the same features. The largest variations between the two low-energy boundary conditions in Figure 9 mostly occurred during the shaded periods, marking times when S-shaped energy structure of the outer radiation belt was observed. Comparing

Figure 10b and Figure 10c suggests that the overestimations of the seed population in the POES low-energy boundary condition, during quiet times, as a result of the S-shaped energy structure, has not had an adverse effect on the model output.

Although mostly similar, there are slight differences between the two model outputs. Following the initial enhancement starting on 7 June, the model run using the POES low-energy boundary condition produced a slightly higher 0.9-MeV electron flux than the model run using the Van Allen Probes low-energy boundary condition. Additionally, the second enhancement starting around 22 June does not extend quite as low in L* for the model run shown in Figure 10b as that in Figure 10c. These variations may be a result of the MLT coverage and rapid L* sampling offered by the POES satellites.

The general agreement between Figure 10b and Figure 10c suggest that the POES low-energy boundary condition would provide a good event-specific low-energy boundary condition for periods outside of the Van Allen Probes mission. Furthermore, another use of the methods presented in this paper would be to provide an alternative event-specific low-energy boundary conditions for events during the Van Allen Probes mission. Comparing the model output obtained from using the POES low-energy boundary condition to the model output from using the Van Allen Probes low-energy boundary condition for the same event would enable the relative importance of changes in the seed population on higher-energy enhancements to be examined. The low-energy boundary condition formulated from POES satellite data may include localized and short-lived enhancements, unseen by the Van Allen Probes. As such, this could potentially lead to better understanding of how the dynamics of the seed population affect flux enhancements.

9. Discussion

The POES satellites operate in low Earth orbit and so measure electrons near the bottom of field lines, relating to low equatorial pitch angles (e.g., ~12° at L* = 3). Additionally, the MEPED detector measures integral electron flux, covering an energy range from 30, 100, or 300 keV up to 2.5 MeV. Sections 6 and 7 showed the results of using these low equatorial pitch angle, integral flux measurements to determine 90° equatorial pitch angle, differential flux for energies in the 100- to 600-keV range, or along a line of constant $\mu = 100$ MeV/G. The comparison of the resulting values to equivalent near-90° differential flux measurements from the MagEIS instrument show that the developed methods work well, considering the challenges involved. For the majority of L* values and energies considered, the average difference between the retrieved flux values and the corresponding MagEIS measurements were less than a factor of 4. Furthermore, it is encouraging that the results of the two methods for converting from integral to differential flux result in similar outputs. Figure 9 shows that the flux from either method overlapped for much of June 2013.

In Figure 7, several periods were identified in the MagEIS data where the electron flux increased with energy. As the MEPED detectors onboard the POES satellites measure integral electron flux, solely using POES data, we were unable to determine occasions when this occurred. A deepening minimum around 300 keV tends to produce a peak at ~800 keV. This peak is included in the integral measurement, but, as we assume that the electron flux falls with increasing energy, we attribute its contribution to an increased flux at the lower-energy values. As a result, when the flux distribution showed this form, the methods presented typically return flux values for energetic electrons that are higher than observed, as shown by Figure 9. The minimum is thought to be formed by the combination of losses due to hiss waves and gradual radial diffusion (Ripoll et al., 2017) and primarily occur during quiet times. For more active periods, when wave acceleration processes are effective (Meredith et al., 2012), we tend to see energetic electron injections and flux energy distributions that do fall with increasing energy. As a result, when the seed population is likely to be an important component to accurately reproduce the ~1-MeV electron flux in radiation belt models, the methods presented in this paper for forming a low-energy boundary condition are unlikely to be affected by S-shaped distributions. Overestimating the seed population during quiet times may cause the model flux at energies very close to the low-energy boundary to be overestimated. However, in the absence of a significant acceleration mechanism, this is unlikely to extend to energies far from the boundary, as evidenced by the 0.9-MeV flux from the BAS Radiation Belt Model using the POES low-energy boundary condition, shown in Figure 10b. During the quiet period from 12 to 20 June 2013, when S-shaped energy structure was observed over a range of L* and the seed population overestimated by the POES low-energy boundary condition, the model result obtained (Figure 10b) is largely similar to the model output where the low-energy boundary condition was supplied by MagEIS observations (Figure 10c).

What is perhaps surprising is how regularly the electron flux rises with increasing energy as well as the L* range over which this was observed. During June 2013 the MagEIS data showed that the assumption was violated for L* = 3.5 to 5.5. The integral flux observed by the POES satellites did not always decrease sharply when the Van Allen Probes MagEIS instrument recorded a sharp drop in the electron flux at energies close to the lower-energy threshold of the integral channel. This agrees with the observations of Reeves et al. (2016) and Ripoll et al. (2016), which suggest that during such periods the flux level at higher energies is maintained, forming minima in the flux energy distributions.

Figure 9 shows that during the first half of June 2013, at L* = 3.5, the 490-keV MagEIS flux rapidly increased twice (on 1 and 7 June). The converted POES flux from both methods 1 and 2 rose for these instances but did not show enhancements to the same extent as the observations. Figures 4 and 6 suggest that for L* > 4.5, the shape parameter of the average pitch angle distribution does not vary notably with activity for any of the electron energies considered. Conversely, for L* values in the 2–4.5 range, the $n(E)$ and $N(E)$ values showed a larger variation with Kp. If the pitch angle distributions for the integral flux during both enhancements in early June were better described by higher $N(E)$ than that of the average distribution for the activity level, the omnidirectional flux used in the conversion would also be higher and may account for the differences observed between the MagEIS flux and the converted values. Likewise if larger $n(E)$ better described the pitch angle distribution for the 490-keV electrons, the 90° pitch angle flux would be underestimated. The pitch angle distributions can take forms that are not described by any of the functions presented in this paper. Gannon et al. (2007) observed so-called butterfly distributions that show a double peak form with a minimum near 90°. While butterfly distributions were not considered when fitting to the average Van Allen Probes pitch angle data, these pitch angle distributions can exist in the radiation belt region (Albert et al., 2017; Zhao et al., 2014b). The occurrence rate of butterfly distributions for 510-keV electrons has been shown to exhibit a local time dependence, with butterfly distributions seen primarily on the night side at $L > 5.5$ (Gannon et al., 2007). Ni et al. (2016) demonstrated a similar nightside bias for butterfly distributions in megaelectronvolt energy electron populations for $L > \sim 5.5$; however, pitch angle distributions have been shown to be largely energy dependent (Zhao et al., 2018) and the findings of Gannon et al. (2007) suggest butterfly distributions occur more readily at $L > 5.5$ for higher-energy electrons. This was also observed by Horne et al. (2003), with butterfly distributions seen at $L = 6$ for electrons greater than 340 keV, while pancake distributions were observed at lower energies. Further work is required to better understand the occurence of butterfly distributions for 100- to 300-keV electrons for L* > 4.5 as previous studies have largely focused on electrons of higher energy. A fully MLT-dependent empirical pitch angle distribution model is beyond the scope of the current study. However, a larger library of potential pitch angle distributions, including MLT variations, may be used to improve the results from the method in future work.

As ratios shown in Figure 8 are primarily greater than one, the methods presented in this paper tend to produce electron flux values moderately less than those observed by MagEIS. It is possible that some of this variation originates in the average pitch angle distributions assumed, as discussed above. Additionally, disparities may arise from the L* mapping of the data as the POES and Van Allen Probes L* values have been calculated using different external field models (Tsyganenko (1995) and Tsyganenko (1989), respectively). The MagEIS and SEM-2 instruments have different designs and ways of operating, and as such, the lower values for the electron flux given from the POES measurements may also arise from instrumentation differences. For L* $\gtrapprox$ 3.7 the average ratios between the MagEIS flux measurements and the electron flux retrieved from the POES measurements are fairly consistent in L* for each energy. As such, the ratio values could potentially be used as a correction factor, which would encompass the aforementioned sources of error, to improve the agreement between the POES retrieved flux and the MagEIS observations, as has been applied in previous work (Meredith et al., 2017).

Figure 9 displays a curious feature of the POES data. A slight diurnal variation can be observed for each of the L* cuts shown. This diurnal fluctuation has been reported by previous authors (Meredith et al., 2016), where it was attributed to sampling effects. The diurnal pattern has been reduced in part by considering only the trapped electron population and correcting measurement times where trapped electrons were only observed by part of the field-of-view (as described in section 2). However, despite this, some daily variation still persists in the POES data. All five POES satellites used in this study exhibit the diurnal fluctuation separately and further work is required to fully understand its origin.

Average pitch angle distributions, formulated using MagEIS data, have been considered in this study to convert the POES data to omnidirectional flux, and to estimate the electron flux at a 90° pitch angle. Where equation (9) was fitted to the average MagEIS equatorial pitch angle distributions, the resulting $n(E)$ values shown in Figure 6 are largely similar to those presented by Shi et al. (2016) (who also assumed the form given by equation (9)). Additionally, the n values from the 100-keV electron differential flux pitch angle distributions are near to the >100-keV N parameters for L* values where a single sine function was used. An agreement between the differential 100-keV n values and the N values for the integral >100-keV flux supports the assumption made in section 3 that allows the pitch angle distributions to be approximated by equation (1), and this is further reinforced by comparing the 300-keV n values to the >300-keV N values. When Shi et al. (2016) considered how the $n(E)$ varied with L (as opposed to L* used in this study), a notable peak in the $n(E)$ values can be observed in the region of $L = 2-4$, with the exact L of the peak depending on both electron energy and activity. This peak in $n(E)$ for L values relating to the slot region is likely associated with the cap distributions named by Zhao et al. (2014a), where a sharp peak in the flux can be seen around a pitch angle of 90° for an otherwise mostly flat distribution. In sections 3 and 5 of the present paper, a second equation involving two sine functions was fitted to pitch angle distributions that displayed this form, and the corresponding L* values were shaded gray in Figures 4 and 6. Generally, for equivalent electron energies and activity levels, the L range for the peak in $n(E)$ shown by Shi et al. (2016) are similar to the L* values where the distribution consisting of two sine functions best fitted the pitch angle distribution. For both the integral and differential flux, the L* values where cap pitch angle distributions were observed reduced with increasing electron energy. The energy dependence in the location of these cap pitch angle distributions agrees with the suggestion that the observed cap pitch angle distributions are formed by hiss waves Lyons et al. (1972).

There are four main benefits of using the methods put forth in this paper to formulate the low-energy boundary condition for radiation belt models from low Earth orbit POES data. First, it enables the low-energy boundary to be calculated for 3-D radiation belt models with a higher temporal resolution than can be achieved with the Van Allen Probes. As such, it enables the importance of short-lived seed population enhancements to be examined. Second, with multiple satellites, a better MLT coverage is given by POES and, in addition to improving the drift average, the retrieved POES data could be used to formulate low-energy boundary conditions for up-and-coming 4-D models. Third, the POES and MetOp satellites present a wealth of data, with SEM-2 coverage spanning ~19 years, enabling event-specific low-energy boundary conditions to be formed for events prior to the start of the Van Allen Probes mission, and likely afterward. Using a realistic low-energy boundary, derived from data, enables better understanding of the role of local acceleration during such events (Tu et al., 2014). Fourth, POES is able to measure the electron flux out to the last closed drift shell. Glauert et al. (2014b) presented a method where the phase space density was set to zero for the outer boundary condition, simulating losses to the magnetopause. By using the methods presented in the current paper to formulate the low-energy boundary condition for an event, and using an outer boundary condition such as that described by Glauert et al. (2014b), the entire radiation belt region could be studied using a radiation belt model. Other uses of the retrieved data set include examining the evolution of the seed population across multiple MLTs. Once the POES data has been converted to differential flux, it can be used to calculate the phase space density. Analysis of the phase space density evolution is a valuable tool to ascertain physical processes active in the radiation belt region (Green & Kivelson, 2004) and the coverage of multiple MLT planes may help to further identify processes affecting the seed population.

10. Summary and Conclusions

Here we have presented a novel method to convert the >30-, >100-, and >300-keV electron flux measurements from the POES satellites at low Earth orbit to differential flux values across a range of energies, at 90° pitch angle. The retrieval process consisted of the following steps.

1. Measurements where the POES satellites observed the trapped electron population were isolated, and when trapped electrons were only observed by part of the MEPED T90 field-of-view, a correction was applied.
2. The POES data were converted to omnidirectional integral flux by assuming that the pitch angle distribution obeyed either a single or double sine form. The required parameters for the conversion to omnidirectional flux were determined by analyzing Van Allen Probes data at a number of L* values and at three levels of Kp.
3. The omnidirectional integral flux measurements were then converted to an omnidirectional differential flux spectrum. Two methods to convert the omnidirectional integral flux readings have been investigated. The

first method employs a library of flux energy distributions returned by the AE9 model, and the second uses a RMC style iterative fitting approach.

4. Lastly, the omnidirectional flux at each energy was converted to 90° directional flux by again assuming that the pitch angle distribution obeyed a single or double sine function, depending on location and energy. The associated shape parameters were found using average pitch angle distributions from level 3 MagEIS data for 100-, 200-, 300-, 500-, and 800-keV electrons, at three levels of Kp and L* = 1.5–5.7.

The results from both methods were compared to observations from the MagEIS instruments onboard the Van Allen Probes. For $L^* \gtrapprox 3.7$, the average difference between the converted POES flux and the MagEIS measurement was less than a factor of 4 for energies 100–600 keV. For $L^* \lessapprox 3.7$, average differences tended to be larger, likely due to pitch angle distributions having a greater dependence on activity for this L* range.

The 90° equatorial pitch angle flux, at a number of L* values, for electron energies following a line of constant $\mu = 100$ MeV/G were computed using the POES data, and the results compared to the equivalent flux from MagEIS. Typically, both methods produce flux values close to the MagEIS measurements, particularly for L* = 4.5–5.5. We suggest that the methods here could be used to formulate event-specific low-energy boundary conditions for radiation belt models in order to better study events outside the time period covered by the Van Allen Probes mission (prior to 2012, and with MetOp data, potentially after the Van Allen Probes are no longer operational) or at L* outside the Van Allen Probes Orbit.

The assumption that the electron flux falls with increasing energy did not always hold, resulting in the flux potentially being overestimated. However, the conditions leading to the breakdown of this assumption primarily occur during quiet times. If POES data were used to generate the low-energy boundary condition for radiation belt models, an overestimation of the seed population during quiet periods is unlikely to dramatically alter model outputs at higher energies.

In conclusion, we have formulated the electron flux at 90° equatorial pitch angle for a number of seed population energies, using integral electron flux measurements taken from POES satellites operating in low Earth orbit. The resulting method can produce data that, for electron energies between 100 and 600 keV, are typically within a factor of 4 of the MagEIS observed levels. The method also enables the reconstruction of the electron differential flux at the equator for the entire period 1998–2018.

Acknowledgments

H. J. A. was supported by NERC Doctoral Training Programme NE/L002507/1. R. B. H. and S. A. G. were supported by NERC National Capability Funding and Natural Environment Research Council (NERC) Highlight Topic grant NE/P01738X/1 (Rad-Sat) and G. D. Z. also acknowledges STFC support. We thank Janet Green for her bow tie analysis software. The authors also acknowledge the NOAA National Geophysical Data Centre for the POES particle data used in this study (https://ngdc.noaa.gov/stp/satellite/poes/dataaccess.html) and give thanks for OMNI database access for both Kp and AE indices. Van Allen probes MagEIS data presented in this paper are available through the Van Allen Probes instrument suite webpages (https://www.rbsp-ect.lanl.gov/science/DataDirectories.php). The BAS-RBM model runs shown in this paper can be downloaded from the UK Polar Data Center at https://data.bas.ac.uk/ (https://doi.org/10.5285/38b0ff75-e0c9-447c-8ddc-cbd4d4e43469).

References

Albert, J. M., Meredith, N. P., & Horne, R. B. (2009). Three-dimensional diffusion simulation of outer radiation belt electrons during the 9 October 1990 magnetic storm. *Journal of Geophysical Research*, *114*, A09214. https://doi.org/10.1029/2009JA014336

Albert, J. M., Starks, M. J., Horne, R. B., Meredith, N. P., & Glauert, S. A. (2017). Quasi-linear simulations of inner radiation belt electron pitch angle and energy distributions. *Geophysical Research Letters*, *43*, 2381–2388. https://doi.org/10.1002/2016GL067938

Allison, H. J., Horne, R. B., Glauert, S. A., & Del Zanna, G. (2017). The magnetic local time distribution of energetic electrons in the radiation belt region. *Journal of Geophysical Research: Space Physics*, *122*, 8108–8123. https://doi.org/10.1002/2017JA024084

Blake, J. B., Carranza, P. A., Claudepierre, S. G., Clemmons, J. H., Crain, W. R., Dotan, Y., et al. (2013). The magnetic electron ion spectrometer (MagEIS) instruments aboard the radiation belt storm probes (RBSP) spacecraft. *Space Science Reviews*, *179*(1), 383–421. https://doi.org/10.1007/s11214-013-9991-8

Boyd, A. J., Spence, H. E., Huang, C.-L., Reeves, G. D., Baker, D. N., Turner, D. L., et al. (2016). Statistical properties of the radiation belt seed population. *Journal of Geophysical Research: Space Physics*, *121*, 7636–7646. https://doi.org/10.1002/2016JA022652

Brautigam, D. H., & Albert, J. M. (2000). Radial diffusion analysis of outer radiation belt electrons during the October 9, 1990, magnetic storm. *Journal of Geophysical Research*, *105*(A1), 291–309. https://doi.org/10.1029/1999JA900344

Carpenter, D. L., & Anderson, R. R. (1992). An ISEE/whistler model of equatorial electron density in the magnetosphere. *Journal of Geophysical Research*, *97*(A2), 1097–1108. https://doi.org/10.1029/91JA01548

Cayton, T. E., Belian, R. D., Gary, S. P., Fritz, T. A., & Baker, D. N. (1989). Energetic electron components at geosynchronous orbit. *Geophysical Research Letters*, *16*(2), 147–150. https://doi.org/10.1029/GL016i002p00147

Evans, D. S., & Greer, M. S. (2004). Polar orbiting environmental satellite space environment monitor-2: Instrument descriptions and archive data documentation (*NOAA Tech. Mem. 93, version 1.4*). Boulder, Colo: Space Weather Prediction Cent.

Gannon, J. L., Li, X., & Heynderickx, D. (2007). Pitch angle distribution analysis of radiation belt electrons based on combined release and radiation effects satellite medium electrons a data. *Journal of Geophysical Research*, *112*, A05212. https://doi.org/10.1029/2005JA011565

Ginet, G. P., O'Brien, T. P., Huston, S. L., Johnston, W. R., Guild, T. B., Friedel, R., et al. (2013). AE9, AP9 and SPM: New models for specifying the trapped energetic particle and space plasma environment. *Space Science Reviews*, *179*(1), 579–615. https://doi.org/10.1007/s11214-013-9964-y

Glauert, S. A., & Horne, R. B. (2005). Calculation of pitch angle and energy diffusion coefficients with the PADIE code. *Journal of Geophysical Research*, *110*, A04206. https://doi.org/10.1029/2004JA010851

Glauert, S. A., Horne, R. B., & Meredith, N. P. (2014a). Three-dimensional electron radiation belt simulations using the BAS radiation belt model with new diffusion models for chorus, plasmaspheric hiss, and lightning-generated whistlers. *Journal of Geophysical Research: Space Physics*, *119*, 268–289. https://doi.org/10.1002/2013JA019281

Glauert, S. A., Horne, R. B., & Meredith, N. P. (2014b). Simulating the Earth's radiation belts: Internal acceleration and continuous losses to the magnetopause. *Journal of Geophysical Research: Space Physics*, *119*, 7444–7463. https://doi.org/10.1002/2014JA020092

Glauert, S. A., Horne, R. B., & Meredith, N. P. (2018). A 30 year simulation of the outer electron radiation belt. *Space Weather*, *16*. https://doi.org/10.1029/2018SW001981

Green, J. C., & Kivelson, M. G. (2004). Relativistic electrons in the outer radiation belt: Differentiating between acceleration mechanisms. *Journal of Geophysical Research*, *109*, A03213. https://doi.org/10.1029/2003JA010153

Höcker, A., & Kartvelishvili, V. (1996). SVD approach to data unfolding. *Nuclear Instruments and Methods in Physics Research Section A: Accelerators, Spectrometers, Detectors and Associated Equipment*, *372*(3), 469–481. https://doi.org/10.1016/0168-9002(95)01478-0

Horne, R. B., Kersten, T., Glauert, S. A., Meredith, N. P., Boscher, D., Sicard-Piet, A., et al. (2013). A new diffusion matrix for whistler mode chorus waves. *Journal of Geophysical Research: Space Physics*, *118*, 6302–6318. https://doi.org/10.1002/jgra.50594

Horne, R. B., Meredith, N. P., Thorne, R. M., Heynderickx, D., Iles, R. H. A., & Anderson, R. R. (2003). Evolution of energetic electron pitch angle distributions during storm time electron acceleration to megaelectronvolt energies. *Journal of Geophysical Research*, *108*(A1), SMP 11–1-SMP 11-13. https://doi.org/10.1029/2001JA009165

Jaynes, A. N., Baker, D. N., Singer, H. J., Rodriguez, J. V., Loto'aniu, T. M., Ali, A. F., et al. (2015). Source and seed populations for relativistic electrons: Their roles in radiation belt changes. *Journal of Geophysical Research: Space Physics*, *120*, 7240–7254. https://doi.org/10.1002/2015JA021234

Kersten, T., Horne, R. B., Glauert, S. A., Meredith, N. P., Fraser, B. J., & Grew, R. S. (2014). Electron losses from the radiation belts caused by EMIC waves. *Journal of Geophysical Research: Space Physics*, *119*, 8820–8837. https://doi.org/10.1002/2014JA020366

Lam, M. M., Horne, R. B., Meredith, N. P., Glauert, S. A., Moffat-Griffin, T., & Green, J. C. (2010). Origin of energetic electron precipitation >30 keV into the atmosphere. *Journal of Geophysical Research*, *115*, A00F08. https://doi.org/10.1029/2009JA014619

Lyons, L. R., Thorne, R. M., & Kennel, C. F. (1972). Pitch-angle diffusion of radiation belt electrons within the plasmasphere. *Journal of Geophysical Research*, *77*(19), 3455–3474. https://doi.org/10.1029/JA077i019p03455

Mauk, B. H., Fox, N. J., Kanekal, S. G., Kessel, R. L., Sibeck, D. G., & Ukhorskiy, A. (2013). Science objectives and rationale for the Radiation Belt Storm Probes mission. *Space Science Reviews*, *179*(1), 3–27. https://doi.org/10.1007/s11214-012-9908-y

McGreevy, R. L. (2001). Reverse monte carlo modelling. *Journal of Physics: Condensed Matter*, *13*(46), R877.

McGreevy, R. L., & Pusztai, L. (1988). Reverse Monte Carlo simulation: A new technique for the determination of disordered structures. *Molecular Simulation*, *1*(6), 359–367. https://doi.org/10.1080/08927028808080958

Meredith, N. P., Horne, R. B., Glauert, S. A., Baker, D. N., Kanekal, S. G., & Albert, J. M. (2009). Relativistic electron loss timescales in the slot region. *Journal of Geophysical Research*, *114*, A03222. https://doi.org/10.1029/2008JA013889

Meredith, N. P., Horne, R. B., Isles, J. D., & Green, J. C. (2016). Extreme energetic electron fluxes in low Earth orbit: Analysis of POES $E > 30$, $E > 100$, and $E > 300$ keV electrons. *Space Weather*, *14*, 136–150. https://doi.org/10.1002/2015SW001348

Meredith, N. P., Horne, R. B., Sandberg, I., Papadimitriou, C., & Evans, H. D. R. (2017). Extreme relativistic electron fluxes in the Earth's outer radiation belt: Analysis of integral IREM data. *Space Weather*, *15*, 917–933. https://doi.org/10.1002/2017SW001651

Meredith, N. P., Horne, R. B., Sicard-Piet, A., Boscher, D., Yearby, K. H., Li, W., & Thorne, R. M. (2012). Global model of lower band and upper band chorus from multiple satellite observations. *Journal of Geophysical Research*, *117*, A10225. https://doi.org/10.1029/2012JA017978

Ni, B., Zou, Z., Gu, X., Zhou, C., Thorne, R. M., Bortnik, J., et al. (2015). Variability of the pitch angle distribution of radiation belt ultrarelativistic electrons during and following intense geomagnetic storms: Van Allen Probes observations. *Journal of Geophysical Research: Space Physics*, *120*, 4863–4876. https://doi.org/10.1002/2015JA021065

Ni, B., Zou, Z., Li, X., Bortnik, J., Xie, L., & Gu, X. (2016). Occurrence characteristics of outer zone relativistic electron butterfly distribution: A survey of Van Allen Probes REPT measurements. *Geophysical Research Letters*, *43*, 5644–5652. https://doi.org/10.1002/2016GL069350

Obara, T., Nagatsuma, T., Den, M., Miyoshi, Y., & Morioka, A. (2000). Main-phase creation of "seed" electrons in the outer radiation belt. *Earth, Planets and Space*, *52*(1), 41–47. https://doi.org/10.1186/BF03351612

Peck, E. D., Randall, C. E., Green, J. C., Rodriguez, J. V., & Rodger, C. J. (2015). POES MEPED differential flux retrievals and electron channel contamination correction. *Journal of Geophysical Research: Space Physics*, *120*, 4596–4612. https://doi.org/10.1002/2014JA020817

Reeves, G. D., Friedel, R. H. W., Larsen, B. A., Skoug, R. M., Funsten, H. O., Claudepierre, S. G., et al. (2016). Energy-dependent dynamics of keV to meV electrons in the inner zone, outer zone, and slot regions. *Journal of Geophysical Research: Space Physics*, *121*, 397–412. https://doi.org/10.1002/2015JA021569

Ripoll, J.-F., Reeves, G. D., Cunningham, G. S., Loridan, V., Denton, M., Santolik, O., et al. (2016). Reproducing the observed energy-dependent structure of Earth's electron radiation belts during storm recovery with an event-specific diffusion model. *Geophysical Research Letters*, *43*, 5616–5625. https://doi.org/10.1002/2016GL068869

Ripoll, J.-F., Santolik, O., Reeves, G. D., Kurth, W. S., Denton, M. H., Loridan, V., et al. (2017). Effects of whistler mode hiss waves in March 2013. *Journal of Geophysical Research: Space Physics*, *122*, 7433–7462. https://doi.org/10.1002/2017JA024139

Rodger, C. J., Carson, B. R., Cummer, S. A., Gamble, R. J., Clilverd, M. A., Green, J. C., et al. (2010). Contrasting the efficiency of radiation belt losses caused by ducted and nonducted whistler-mode waves from ground-based transmitters. *Journal of Geophysical Research*, *115*, A12208. https://doi.org/10.1029/2010JA015880

Rodger, C. J., Clilverd, M. A., Green, J. C., & Lam, M. M. (2010). Use of POES SEM-2 observations to examine radiation belt dynamics and energetic electron precipitation into the atmosphere. *Journal of Geophysical Research*, *115*, A04202. https://doi.org/10.1029/2008JA014023

Roederer, J. G. (1970). *Dynamics of geomagnetically trapped radiation* (1st ed.)., vol. 2. Heidelberg, New York: Springer-Verlag Berlin.

Sandberg, I., Daglis, I. A., Anastasiadis, A., Buhler, P., Nieminen, P., & Evans, H. (2012). Unfolding and validation of SREM fluxes. *IEEE Transactions on Nuclear Science*, *59*, 1105–1112. https://doi.org/10.1109/TNS.2012.2187216

Shi, R., Summers, D., Ni, B., Fennell, J. F., Blake, J. B., Spence, H. E., & Reeves, G. D. (2016). Survey of radiation belt energetic electron pitch angle distributions based on the Van Allen Probes MagEIS measurements. *Journal of Geophysical Research: Space Physics*, *121*, 1078–1090. https://doi.org/10.1002/2015JA021724

Shprits, Y. Y., Subbotin, D., Drozdov, A., Usanova, M. E., Kellerman, A., Orlova, K., et al. (2013). Unusual stable trapping of the ultrarelativistic electrons in the Van Allen radiation belts. *Nature Physics*, *9*, 699–703.

Spence, H. E., Reeves, G. D., Baker, D. N., Blake, J. B., Bolton, M., Bourdarie, S., et al. (2013). Science goals and overview of the Radiation Belt Storm Probes (RBSP) energetic particle, composition, and thermal plasma (ECT) suite on NASA's Van Allen Probes mission. *Space Science Reviews*, *179*(1), 311–336. https://doi.org/10.1007/s11214-013-0007-5

Thébault, E., Finlay, C. C., Beggan, C. D., Alken, P., Aubert, J., Barrois, O., et al. (2015). International geomagnetic reference field: The 12th generation. *Earth, Planets and Space*, *67*(1), 79. https://doi.org/10.1186/s40623-015-0228-9

Tsyganenko, N. (1989). A magnetospheric magnetic field model with a warped tail current sheet. *Planetary and Space Science*, *37*(1), 5–20. https://doi.org/10.1016/0032-0633(89)90066-4

Tsyganenko, N. A. (1995). Modeling the Earth's magnetospheric magnetic field confined within a realistic magnetopause. *Journal of Geophysical Research*, *100*(A4), 5599–5612. https://doi.org/10.1029/94JA03193

Tu, W., Cunningham, G. S., Chen, Y., Henderson, M. G., Camporeale, E., & Reeves, G. D. (2013). Modeling radiation belt electron dynamics during GEM challenge intervals with the dream3d diffusion model. *Journal of Geophysical Research: Space Physics*, *118*, 6197–6211. https://doi.org/10.1002/jgra.50560

Tu, W., Cunningham, G. S., Chen, Y., Morley, S. K., Reeves, G. D., Blake, J. B., et al. (2014). Event-specific chorus wave and electron seed population models in DREAM3D using the van allen probes. *Geophysical Research Letters*, *41*, 1359–1366. https://doi.org/10.1002/2013GL058819

Vampola, A. (1997). Outer zone energetic electron environment update. In *Conference on the High Energy Radiation Background in Space. Workshop Record*, IEEE, pp. 128–136. https://doi.org/10.1109/CHERBS.1997.660263

Wang, C., Ma, Q., Tao, X., Zhang, Y., Teng, S., Albert, J. M., et al. (2017). Modeling radiation belt dynamics using a 3-D layer method code. *Journal of Geophysical Research: Space Physics*, *122*, 8642–8658. https://doi.org/10.1002/2017JA024143

Yando, K., Millan, R. M., Green, J. C., & Evans, D. S. (2011). A monte Carlo simulation of the NOAA POES medium energy proton and electron detector instrument. *Journal of Geophysical Research*, *116*(A10231). https://doi.org/10.1029/2011JA016671

Zhao, H., Friedel, R. H. W., Chen, Y., Reeves, G. D., Baker, D. N., Li, X., et al. (2018). An empirical model of radiation belt electron pitch angle distributions based on Van Allen Probes measurements. *Journal of Geophysical Research: Space Physics*, *123*, 3493–3511. https://doi.org/10.1029/2018JA025277

Zhao, H., Li, X., Blake, J. B., Fennell, J. F., Claudepierre, S. G., Baker, D. N., et al. (2014a). Characteristics of pitch angle distributions of hundreds of keV electrons in the slot region and inner radiation belt. *Journal of Geophysical Research: Space Physics*, *119*, 9543–9557. https://doi.org/10.1002/2014JA020386

Zhao, H., Li, X., Blake, J. B., Fennell, J. F., Claudepierre, S. G., Baker, D. N., et al. (2014b). Peculiar pitch angle distribution of relativistic electrons in the inner radiation belt and slot region. *Geophysical Research Letters*, *41*, 2250–2257. https://doi.org/10.1002/2014GL059725